Contributions to Geophysics and Geodesy Vol. 52/1, 2022 (1–56)

Quantification of groundwater storage variation in Himalayan & Peninsular River basins correlating with land deformation effects observed at different Indian cities

Tandrila SARKAR[1], Anuradha KARUNAKALAGE[2,3], Suresh KANNAUJIYA[4,*], Charan CHAGANTI[4]

[1] Indian Institute of Technology (Indian School of Mines) Dhanbad, Jharkhand, 826004, India

[2] International Water Management Institute (Headquarters), Colombo, Western Province, 10120, Sri Lanka

[3] Centre for Space Science and Technology Education in Asia and the Pacific, Indian Institute of Remote Sensing, Indian Space Research Organisation, Dehradun, Uttarakhand, 248001, India

[4] Indian Institute of Remote Sensing, Indian Space Research Organisation, Dehradun, Uttarakhand-248001, India

Abstract: Groundwater is a significant resource that supports almost one-fifth population globally, but has been is diminishing at an alarming rate in recent years. To delve into this objective more thoroughly, we calculated interannual (2002–2020) GWS (per grid) distribution using GRACE & GRACE-FO (CSR-M, JPL-M and SH) Level 3 RL06 datasets in seven Indian river basins and found comparatively higher negative trends (-20.10 ± 1.81 to -8.60 ± 1.52 mm/yr) in Basin 1–4 than in Basin 5–7 (-7.11 ± 0.64 to -0.76 ± 0.47 mm/yr). After comparing the Groundwater Storage (GWS) results with the CHIRPS (Climate Hazards Group Infrared Precipitation with Stations) derived SPI (Standardized Precipitation Index) drought index, we found that GWS exhausts analogously in the same period (2005–2020) when SPI values show improvement (~ 1.89–2), indicating towards wet condition. Subsequently, the GWSA time series is decomposed using the STL (Seasonal Trend Decomposition) (LOESS Regression) approach to monitor long-term groundwater fluctuation. The long term GWS rate (mm/yr) derived from three GRACE & GRACE-FO solutions vary from -20.3 ± 5.52 to -13.19 ± 3.28 and the GWS mass rate (km^3/yr) lie in range of -15.17 ± 4.18 to -1.67 ± 0.49 for basins 1–3. Simultaneously, in basin 4–7 the GWS rate observed is -8.56 ± 8.03 to -0.58 ± 7.04 mm/yr, and the GWS mass rate differs by -1.71 ± 0.64 to -0.26 ± 3.19 km^3/yr. The deseasonalized GWS estimation (2002–2020) states that Himalayan River basins 1,2,3 exhibit

*corresponding author, e-mail: skannaujiya@gmail.com

doi: 10.31577/congeo.2022.52.1.1

high GWS mass loss (-260 to -35.12 km^3), with Basin 2 being the highest (-260 km^3). Whereas the Peninsular River basin 4,6,7 gives moderate mass loss value from -26.72 to -23.58 km^3. And in River basin 5, the GWS mass loss observed is the lowest, with a value of -8 km^3. Accordingly, GPS (Global Positioning System) and SAR (Synthetic Aperture Radar) data are considered to examine the land deformation as an effect due to GWS mass loss. The GPS data acquired from two IGS stations, IISC Bengaluru and LCK3 Lucknow, negatively correlates with GWS change, and the values are ~ -0.90 to ~ -0.21 and ~ -0.7 to -0.4, respectively. Consequently, correlation between GWS mass rate (km^3/yr) and the SAR (Sentinel-1A, SBAS) data procured from Chandigarh, Delhi, Mehsana, Lucknow, Kolkata and Bengaluru shows $\sim 72-48\%$ positively correlated area (PCA). The vertical velocity ranges within ~ -94 to -25 mm/yr estimated from PCA. There is an increase in population (estimated 2008–2014) in Basin 1 & 2. Likewise, the correlation coefficient (ρ) between GWS change and the irrigational area is positive in all seven basins indicating significant depletion in GWS due to an uncalled hike in population or irrigational land use. Similarly, the positive linear regression (R^2) in Basins 1–3 also indicates high depletion in GWS. But basins 4–7 observe negative linear regression even after increasing population, which implies a control on the irrigational land use, unable to determine the GWS change at local scale and heterogeneous aquifer distribution. Therefore, if such unsystematic groundwater storage variation is not controlled on time, then very soon in the future, India might reach a deadlock state of water shortage.

Key words: GRACE & GRACE-FO, SPI, STL-deseasonalization, GPS, SAR, correlation coefficient

1. Introduction

Since the Green revolution took place in 1960, agriculture has become an essential source of salvation for millions of Indian farmers. As crops feed and suffice the hunger of India's ever-increasing population, these paddies, in return, get their nourishment from groundwater. But over the last three decades, there has been tremendous exhaustion in groundwater storage rate, which has increased the pressure of over-extraction and has also resulted in land subsidence.

The backbone of India's economy needs an adequate amount of rainfall along with sufficient groundwater recharge. Rainfall infiltration takes place efficiently in porous litho-units like sand and gravel. Seasonal variation influences the seepage rate or infiltration; for instance, a warmer season comparatively allows less hindrance in seepage than cold weather (*Priyan, 2015; Peiris and Seneviratne, 2010*). In certain years when rainfall

is heavy and continual, the depth of the water table confides to a shallow level, which goes deeper in case of poor rainfall periods (*Seeyan et al., 2014*). The rainfall distribution in the Indian subcontinent is dominated by tropical monsoon, which varies from year to year. In this context, conditions like drought and water scarcity encompass at least 28% of India's geographical terrain, which is 1.07 million km^2 (*Samra, 2004; Mishra and Singh, 2010*). India's history of drought (having high frequency) follows the chronology from 1891–1920; 1965–190; 1999–2012, resulting in cataclysmic consequences (*NRAA, 2013*). *Wilhite and Glantz (1985)* classified drought into four categories; meteorological, hydrological, agricultural and subeconomic. As monsoon season in India coincides with the Kharif (June–September) and Rabi (October–April) season, groundwater pumping escalates during these periods. The extreme variation in groundwater storage usually results from either floods or droughts (*Van Loon, 2015*). Droughts befall due to three primary reasons: 'i.e.,' deficiency in rainfall's actual distribution & intensity and increasing demand for surplus water and storage (*Asadi Zarch et al., 2015*).

The increase in population and living standards have exacerbated industrialization, new farming techniques, and excessive groundwater pumping (Fig. S6). Several eminent researchers have conducted different studies on the drought aspects to mitigate the changes in climate/monsoonal conditions prevailing in India. For instance, how acute recession in substantial rainfall amount and duration can convert an area into a drought zone, and how SPI (Standardized Precipitation Index) helps to characterize droughts in different Indian regions (*Parthasarathy et al., 1987; Bhuiyan et al., 2006; Jain et al., 2015*).

SPI is a drought characterization index (*McKee et al., 1993*) that follows a statistical method, thereby analysing the rainfall variations. It is quite versatile and has proved to be a successful indicator for agriculture, water resources and groundwater management in Africa, China, the USA, India (*Spinoni et al., 2018; Cheo et al., 2012; Dhakar et al., 2013*). SPI estimation is carried out using a newly launched satellite data and high-resolution precipitation product in amalgamation with rain gauge analysis known as CHIRPS (Climate Hazards Group Infrared Precipitation with Stations). The CHIRPS holds potentiality and complies with its application in different parts of Asia (*Funk et al., 2015*).

Groundwater portrays a pivotal role as the staple source for irrigation, drinking, domestic and industrial purposes, whose consumption rate has tripled to 33,100,000 ha (1970–1999) (*McGuire, 2009*). This global asset has always adhered to its duties, but due to overexploitation in recent times, it has become a threat to societal and ecosystem development (*Foster and Loucks, 2006*). Thus, it is imperative to balance the increasing population and the consumption rate of groundwater (*Gleeson et al., 2012*). Groundwater recharge is a prolonged process, and if its deterioration rate continues by this rate, it won't be easy to reach the previous groundwater rate. The excessive use of groundwater has already started showing its results ', i.e.,' depletion in groundwater level at some places by 100 m (*Scanlon et al., 2012*). Such depletion is equally detectable both in plain-valley and hilly areas (*Mukherjee et al., 2015*). Also, to quantify groundwater storage variation over a large extent, an area's geology needs to be understood thoroughly along with a dense network of wells. Whereas, in a small area, a limited number of well observations will do the work (*Döll et al., 2014; Haque et al., 2020*). According to CGWB/UN, North India is facing the most water crisis in the world. Recently to irrigate the parched areas of South India, certain water resources are diverted from North India. All these difficulties are faced by climate change and abrupt human intervention (*CGWB, 2012; Kumar et al., 2007; Jasrotia et al., 2019*).

The GRACE (Gravity Recovery and Climate Experiment, 2002–2017)/ GRACE-FO (Gravity Recovery and Climate Experiment – Follow-On, 2018–till date) is a twin satellite mission that measures the temporal variation in Earth's gravity (*Rodell and Famiglietti, 2002; Tapley et al., 2004*). Research has shown how GRACE has successfully proved to detect and measure the changes in groundwater (mainly depletion). GRACE-FO is the successor of GRACE mission which uses an improved parameter, LRI (Laser Ranging Interferometer) for measuring the fluctuation more precisely. For instance, the observation in the Ganga basin (*Panda et al., 2020*), Northwest India (*Long et al., 2017*), Gujarat (*Chinnasamy et al., 2013; Karunakalage et al., 2021*), Northern plains & other parts of India (*Rodell et al., 2007; Sarkar et al., 2020*). The GRACE results are also validated with the ground observations (well data) or GPS (Global Positioning System) to improve the algorithm and justify the TWS (Terrestrial Water Storage)/groundwater change. Likewise, the GLDAS/Global Land Assimilation (0.25°) runs glob-

ally and measures soil moisture, surface water runoff and snow water equivalent. The integration of GRACE and GLDAS over the Ganga-Brahmaputra basin is a flourishing example showing significant GWS change (*Rodell et al., 2009*). Subsequently, the GPS and GRACE integration show a 75.6% correlation factor and 28.9% weighted root mean square reduction, thereby determining the TWS change more efficiently (*Wang et al., 2017*).

The extreme TWS changes can also lead to crustal deformation or displacement at GPS reference points. Consequently, to cope with the rising population, groundwater is getting exploited drastically, leading to many harmful consequences like land subsidence, ecosystem casualties, structural demolition etc. (*Whiteman et al., 2010*). Certain conventional approaches (extensometers, traditional levelling etc.) were used to measure the land subsidence induced by excessive groundwater use (*Huang et al., 2012*). But these measures failed and worked only in a limited spatial extent of tens of kilometres. The Interferometric Synthetic Aperture Radar (InSAR) geospatial data come in for the rescue. It has already given its best attempt in the Central Valley of California for identifying land subsidence at a large scale aggravated due to the high rate of groundwater pumping, thus imposing g threat to buildings located there (*Ojha et al., 2019; Vasco et al., 2019*). The land subsidence or ground deformation indirectly measures the variation within an aquifer, and InSAR has better spatial resolution than geospatial gravity observation data. Along with that, the poroelastic or poroplastic property of aquifer response to the change in volume/mass of water present in the aquifer (*Hoffmann et al., 2003; Chaussard et al., 2014*). Some land deformation studies carried out by SAR using Sentinel-1 data have given favourable results (*Bui et al., 2021; Chen et al., 2020*). Sentinel-1 data can efficiently image the target location every 6 days, has ESA approved global coverage and 5 m spatial resolution (*Torres et al., 2012*).

Thus, India ranks first in the list of excessive groundwater extraction, which is the combined rate of countries like the USA and China. Agriculture in India consumes the maximum percentage of groundwater, and reports have stated drastic depletion of this non-renewable resource in various Indian states (*Margat and Van der Gun, 2013; Bhanja et al., 2017; Mukherjee et al., 2015*). Some substantial groundwater strategies have been taken up in some Indian regions showing comparative groundwater replenishment (*Bhanja et al., 2017*). This research focuses on estimating groundwater stor-

age (GWS) variation using GRACE/GRACE-FO at seven river basins and how the GWS change leads to land deformation in six prominent Indian cities (Delhi, Mehsana, Chandigarh, Lucknow, Kolkata and Bengaluru). The effect of drought estimated using CHIRPS-SPI affecting the GWS rate is also taken into consideration. Furthermore, the results of GRACE-GWS mass loss are correlated with GPS and Sentinel 1A derived vertical velocity for better validation.

2. Study Area

2.1. Physiography of Indian rivers

India is situated in South Asia and is bounded by the Indian Ocean, the Arabian Sea and the Bay of Bengal in the South, Southwest and Southeast, respectively (*Misra et al., 2007*). The Himalayan rivers encompass the North, West & Eastern states, while the rivers flowing through Central and South India is known as Peninsular rivers having steeper gradient, thus preventing the floods (*Aggarwal et al., 2004*). Our relationship with the river system is quite intimate; rivers support the livelihood of the Indian population by providing to industry, domestic and agricultural purposes (Fig. S7). The Himalayan rivers originated from the glacier itself and were fed by both snow water and monsoonal rains. On the other hand, the Peninsular rivers are fed by the Northeast and Southwest monsoon, the main source of annual precipitation in Central and South India.

In this study, we have considered seven basins covering both the Himalayan and peninsular river systems. From Fig. 1, each basin is characterized per unique number termed as Basin point. Now let's discuss the significance of these basins; Basin 1 includes west-flowing rivers of Kutch & Saurashtra, including Luni, along with the five rivers flowing in Punjab (Ravi, Chenab, Jhelum, Sutlej and Beas). Basin 2 includes the Ganga-Brahmaputra rivers. In contrast, Basin 3 comprises Meghna-Brahmaputra-Ganga rivers, and all these three Basin point belongs to Himalayan-river system. The Basin 4–7 falls under the Peninsular-river group. Basin 4 includes Mahanadi and some small rivers like Subarnarekha, Brahmani & Baitarini. Basin point 5 comprises Godavari, Tapi and Narmada rivers. Basin point 6 has only the river Krishna, and Basin point 7 constitute the Pennar, Kaveri and east-flowing rivers lying between the Pennar and Kaveri.

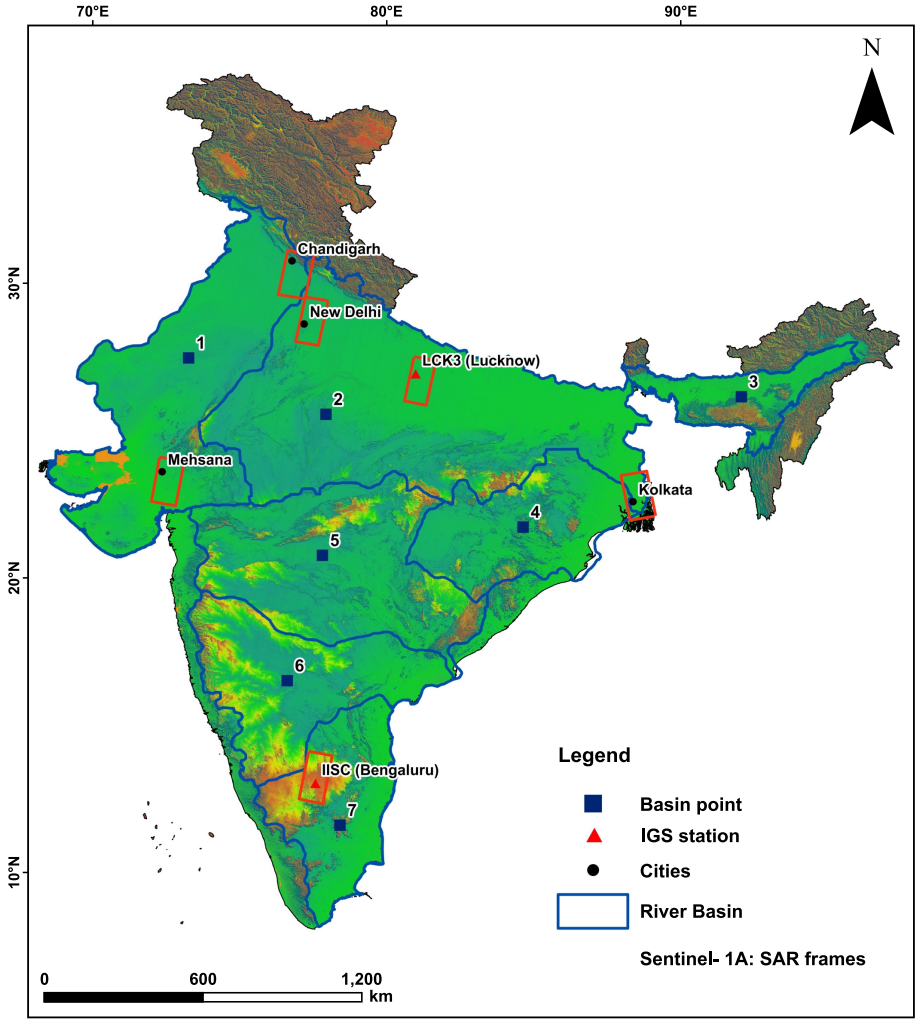

Fig. 1. The study area comprises seven basin points (1–7) bordered by dark blue lines indicating the basin itself, two IGS stations (IISC & LCK3) located in Bengaluru and Lucknow, Sentinel 1A SAR frames with red colour border placed over Indian cities; Chandigarh, Delhi, Lucknow, Mehsana, Kolkata and Bengaluru.

2.2. Geology of the rivers and their aquifer distribution in India

The geology of Himalayan rivers comprises metamorphic rocks of the Precambrian age like gneiss, quartzite and metamorphosed limestone, sand-

stones and shales of Palaeozoic-Mesozoic age, mafic effusive of Mesozoic and Tertiary era and Pb, Hg, As, Illite and Kaolinite (*Huizing, 1971*). Also, the concretions present within the calcareous sediments are called Kankar locally. *CGWB (2012)* reports that alluvium and sandstone aquifer distribution in North Indian rivers is highly porous & permeable and has proved good groundwater storage.

The geology of Peninsular rivers is composed of Dharwar metamorphic rocks (with mineral assemblage phyllite, biotite, kyanite, staurolite and hornblende), Peninsular Granite, Closepet Granite and Charnockites (*Naqvi et al., 1988*). Along with Dharwar Formation, the Cuddapah group, Kurnool group and Deccan traps also constitute the geology of this coastal region. According to *CGWB (2012)* reports, the aquifer distribution is basalt and Banded Gneissic Complex (BGC) in Central and South India, respectively. The basalts are volcanic rock and serve as good groundwater storage, while BGC is poorly permeable. Therefore, South India is characterized by heterogeneous solid aquifer types (BGC) (*Hora et al., 2019*).

3. Data and Methods

The different data and methods used in this research work have been characterized distinctly with the help of a schematic diagram or flowchart (Fig. S1).

3.1. Rainfall and drought characterization from SPI index using CHIRPS

The variation in rainfall intensity both spatially and temporally is essential to monitor drought and study climate change. CHIRPS (Climate Hazards Group Infrared Precipitation with Stations) is an integrated creation between USGS Earth Resources Observation and Science (EROS) Centre is a quasi-global, 0.05° resolution, and provides daily monthly and pentad precipitation data. CHIRPS delivers a contemporary dataset to evaluate drought, early warning signatures and trend analysis. The preliminary objective behind its launch is to study the early warning of famine in the United States (FEWS NET; United States Agency for International Development Famine Early Warning Systems Network). CHIRPS is built on that approach which is successful as TIR (Thermal Infrared) precipitation prod-

uct, 'i.e.,' Rainfall estimate (REF2) of national oceanic and Atmospheric Administration (NOAA) and University of Reading's TAMSAT African Rainfall Climatology and Time Series (TARCAT) /African Rainfall Climatology. It uses the TMPA3B42 v7 (tropical Rainfall measuring Mission Multi-Satellite Precipitation Analysis, version 7) for quantifying the rainfall estimate of global CCD (Cold Cloud Duration) and a smart interpolation technique from climatology of high resolution that works with an anomaly. CHIRPS produces two unique products by incorporating the data obtained from stations in the process of 2 phases. In the first phase, the product received (initial one) have two days lag, very few and scattered GTS (Global Telecommunication System) gauge data of World Meteorological Organization amalgamated with each pentad (6 pentads are there in a calendar month) CCD rainfall estimates. The second phase is the final one having lag for three weeks and contains station data collected on a monthly (and pentad) basis which is blended with high-resolution CCD rainfall estimates (monthly & pentad). It produces fields similar to GPCC (Global Precipitation Climatology Centre) or CRU (University of East Anglia's Climate Research Unit) gridded data. Therefore, CHIRPS is a combination of data like GPCC (interpolated gauge data) and REF2 (sporadic gauge and satellite product) (*Funk et al., 2015*).

SPI (Standardized Precipitation Index) index is developed by the integrated effort of Tom McKee, Nolan Doesken, and John Kleist of Colorado Climate Centre, 1993 (*McKee et al., 1993*) helps in evaluating the drought condition which appears when the rate of the seasonal rainfall decreases from the substantial quantity (*Thomas et al., 2014*). It is an evolving parameter that has accomplished quite a few case studies (*Dhakar et al., 2013*) globally. The likely precipitation occurrence for any time duration is calculated on a 1-, 3-, 6-, 9- and 12-month time scale. SPI value is obtained from Eq. (1), and the resulted values vary from $-2 \leq \mathrm{SPI} \leq 2$, deciding the drought category as suggested by *McKee et al. (1993)*. For instance, if SPI value is ≥ 2 then it is extremely wet (no drought condition); 1.50 – 1.99 (severely wet); 1.00 – 1.49 (moderately wet); 0 – 0.99 (mildly wet); −0.99 – 0 (mild drought), −1.9 – (−)1 (moderate drought), −1.99 – (−)1.50 (severe drought) and < 2 (extreme drought).

$$ {}^{t}_{\mathrm{grid}}\mathrm{SPI} = \frac{X - \bar{X}_t}{\sigma}\,, \tag{1} $$

[t is the time scale of the precipitation probability distribution (6-months), $\bar{X}_t$ is the mean value for the 6 months, and σ is the standardized deviation of t months probability distribution]. SPI is estimated using the R studio function.

For this study, we have considered the 6-month time scale for SPI calculation from 2002–2020 using CHIRPS (v 2.0) datasets because SPI-6 is quite sensitive for studying the seasonal and inter-seasonal rainfall variation. In SPI-6, the precipitation of the current month is compared with the exact

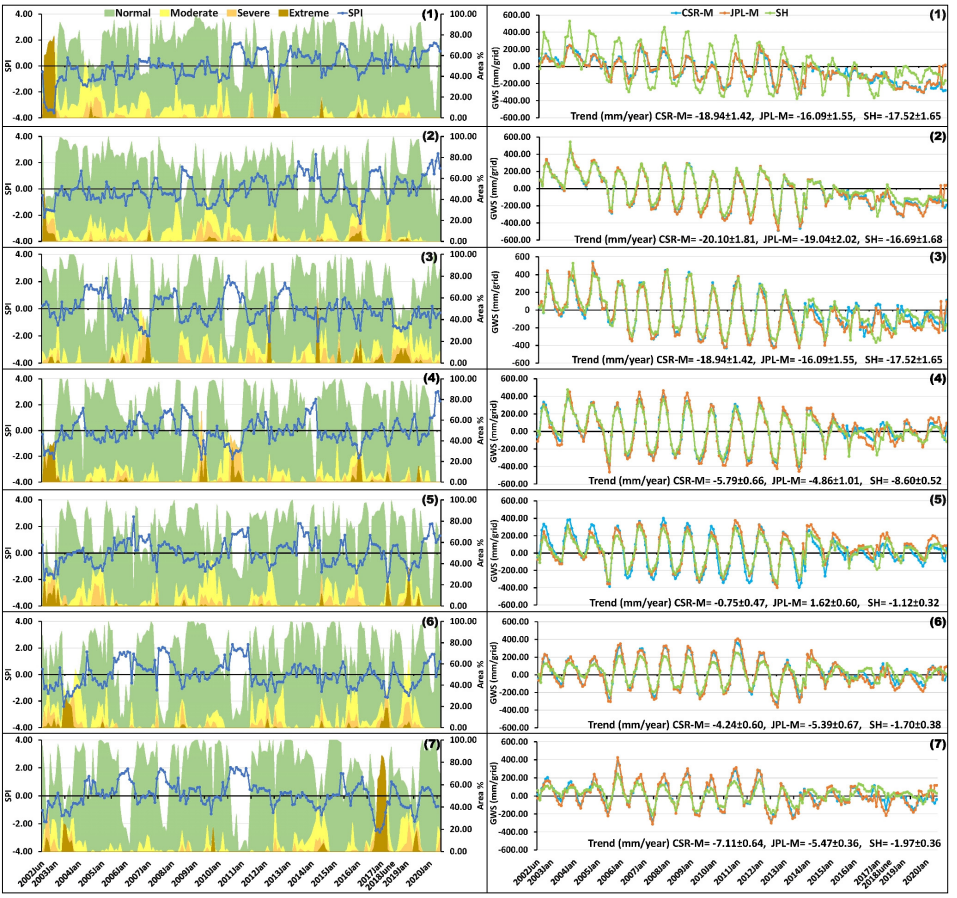

Fig. 2. (a) Standardized Precipitation Index is showing drought variation over the years 2002–2020. (b) Variation in GWS (mm/grid) from 2002–2020 in seven river basins (Basin 1–7) using all the three datasets (CSR-M, JPL-M, SH).

period of six months from previous years. For example, the SPI value at the end of September is compared with total precipitation of the same period of six months (April–September) from preceding years. We have summed up the area of grids/pixels/cells having the same range of SPI value, thereby characterizing drought intensity variation in the seven basins (Fig. 2a).

3.2. Groundwater Storage (GWS) Change estimation from GRACE & GRACE-FO (SH, CSR-M, JPL-M) satellite data

The GRACE & GRACE-FO mission monitored the changes in the water mass at land, ocean and ice sheets (*Reager et al., 2016; Velicogna et al., 2020*). These measurements have made it quite easy to perceive the interannual variation and long-term changes in water mass. Three different gridded GRACE (2002–2017)/GRACE-FO (2018–till date) datasets, SH (1°), CSR-M (0.25°), JPL-M (0.5°), is used for the estimation of GWS from 2002–2020 (Fig. 3). All these three datasets belong to Level 3 RL06 (Table S1).

The Level 3 RL-06 data product has provided the monthly anomalies of terrestrial water storage (TWS) changes which are typically computed related to time-mean baseline of 2004–2009 including all months. For effective comparison, CSR-M data is converted to the same resolution as JPL-M, whereas the SH data are taken from all the three processing centres (CSR, JPL and GFZ) are averaged together (Fig. S1) for effective study. The constraints of CSR-M are based only on GRACE, unlike the JPL-M which is based on both GRACE and geophysical model like hydrology or ocean models. For CSR-M, it is $\sim 41,000$ equal-area (12,400 km^2) hexagonal grids all over the globe, and JPL-M, it is ~ 10 times fewer grids than CSR-M (*Save et al., 2016; Watkins et al., 2015; Scanlon et al., 2016*). By comparing the mascon solutions with Spherical Harmonics, SH fails to differentiate between land and oceans signal leaks and decreasing signal amplitudes. For instance, JPL and CSR-M showed greater signals than SH while analysing the TWSA/GWSA trends in USA and Indian groundwater depletion areas (*Save et al., 2016*). In this context, we have carried out scatter plots of JPL-M and SH in respect to CSR-M for understanding the relations among the three datasets by estimating linear regression slope (r^2) and correlation coefficient (ρ). The estimated values are then categorized with basin size as large (area ~ 400000 km^2), medium (area ~ 200000 km^2) and small

($100000\,\mathrm{km}^2 \leq$ area $< 200000\,\mathrm{km}^2$) to express the results in terms of basin-scale (Table 1). From each month's dataset file, Cl_m and Sl_m are a set of spherical harmonics used to produce a region's gravity anomaly. Along with these spherical harmonics, the surface mass density is calculated with the help of Eq. (2) (*Wahr et al., 1998*):

$$\Delta\sigma\left(\theta,\phi\right) = \frac{a\rho_e}{3\rho_w}\sum_{n=0}^{\infty}\left(\frac{2n+1}{1+k_n}\right)\times \times \sum_{m=0}^{n}\left\{\left[\Delta C_n^m\cos\left(m\phi\right)+\Delta S_n^m\sin\left(m\phi\right)\right]\bar{P}_n^m(\cos\,\theta)\right\}, \tag{2}$$

[θ is latitude; ϕ is the longitude; a is the radius of Earth; ρ_e is the average density of the Earth, ρ_w is the density of water; k_n is load love number which is at degree n; $\bar{P}_n^m$ is fully normalized Legendre function with degree n

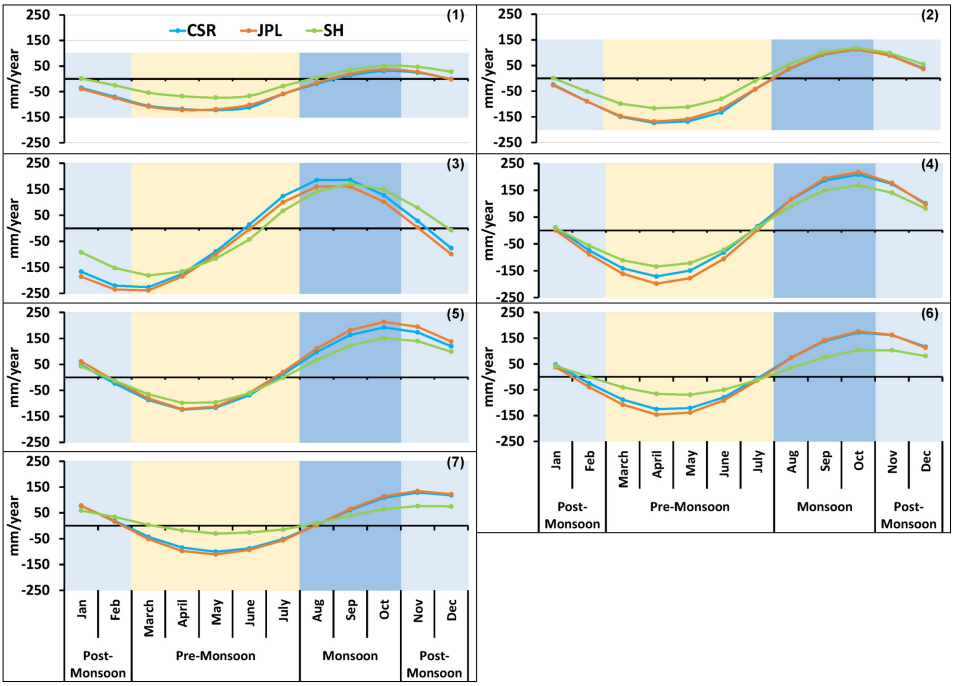

Fig. 3. The seasonal (pre-, co-, post-monsoon) variation in GWS showing decreasing GWS trend in the post (Jan–Feb) and pre-monsoon months and increasing GWS trend in co and post-monsoon months (Nov–Dec).

and order m; C_n^m and ΔS_n^m are the changes of monthly Stokes coefficients]. A decorrelation filter and 300 km Gaussian smoothening are applied for noise correction of data (*Swenson and Wahr, 2006; Jekeli, 1981*).

Table 1. The long term and short term GWS rate and GWS mass rate variation estimated from three different GRACE & GRACE-FO solutions. Statistical relationship among JPL-M and SH with respect to CSR-M. Characterizing the derived results as the basin areas (large, medium and small) using scatter plots. The correlation was carried out between GWS and rainfall measurements at each basin.

GWS rate (mm/yr) and GWS mass rate (km³/year)								
Component	Solution	Basin Point						
		Large			Medium			Small
		2	1	5	6	4	7	3
Long term trend (mm/year)	CSR-M	−20.3	−18.99	−0.58	−4.09	−5.64	−7.04	−14.70
	JPL-M	−18.99	−16.01	1.83	−5.26	−4.71	−5.43	−18.95
	SH	−16.72	−13.19	−1.06	−1.73	−8.56	−2.19	−17.47
Long term trend (km³/year)	CSR-M	−15.17	−9.60	−0.26	−1.32	−1.45	−1.71	−1.67
	JPL-M	−14.39	−8.10	0.83	−1.69	−1.21	−1.32	−2.16
	SH	−12.67	−6.67	−0.48	−0.56	−2.20	−0.53	−1.99
Short term trend (mm/month)	CSR-M	−1.68	−1.57	−0.01	−0.29	−0.46	−0.59	−1.24
	JPL-M	−1.65	−1.38	0.20	−0.42	−0.41	−0.47	−1.66
	SH	−1.44	−1.11	−0.10	−0.15	−0.75	−0.21	−1.51
Short term trend (km³/month)	CSR-M	−1.27	−0.79	−0.01	−0.09	−0.12	−0.14	−0.14
	JPL-M	−1.25	−0.70	0.09	−0.13	−0.11	−0.11	−0.19
	SH	−1.09	−0.56	−0.04	−0.05	−0.19	−0.05	−0.17
Relativity Parameters with CSR-M								
r^2 with CSR-M	JPL-M	0.98	0.93	0.98	0.97	0.97	0.94	0.96
	SH	0.94	0.91	0.95	0.91	0.95	0.76	0.87
ρ with CSR-M	JPL-M	0.99	0.96	0.99	0.99	0.98	0.97	0.98
	SH	0.98	0.98	0.98	0.95	0.97	0.88	0.93
Correlation between GRACE GWS and Precipitation								
Period	Solution	Basin Point						
		1	2	3	4	5	6	7
2002–2007	CSR-M	0.17	0.28	0.52	0.37	0.33	0.28	0.33
	JPL-M	0.22	0.28	0.53	0.37	0.33	0.31	0.34
	SH	0.50	0.30	0.34	0.37	0.30	0.24	0.26
2008–2013	CSR-M	0.10	0.21	0.50	0.32	0.24	0.30	0.27
	JPL-M	0.12	0.23	0.53	0.33	0.26	0.31	0.29
	SH	0.54	0.23	0.35	0.34	0.24	0.30	0.26
2014–2020	CSR-M	−0.19	−0.34	0.38	−0.33	−0.48	−0.36	−0.11
	JPL-M	−0.15	−0.28	0.26	−0.19	−0.45	−0.23	0.00
	SH	−0.05	−0.51	−0.41	−0.58	−0.63	−0.74	−0.51

The monthly GRACE & GRACE-FO datasets for 2002–2020 period from the Centre for Space Research at university of Texas, Austin (CSR) has been used in this study. The TWS is estimated using the Mass concentration blocks (mascons) approach. Implementation of geophysical constraints is much easier and rigorous approach in mascons (*Scanlon et al., 2016*). The grid used in RL06 mascon solution is hexagonal tiles which spans across the coastline, and are split into two tiles along the coastline to reduce leakage between ocean and land signals. The native resolution of CSR mascon RL06 is $1^\circ \times 1^\circ$ represented on a $1/4$ degree longitude-latitude grid. These solutions are computed in presence of regularization constraints that are derived solely from GRACE & GRACE-FO satellite information. The Tikhonov regularization and L-ribbon approach is used to estimate the regularization parameter. As no additional empirical de-stripping, filtering or smoothing is required here so these solutions are applicable in several fields of scientific interests. The anomalies computed for CSR mascon RL06 are relative to mean baseline of 2004–2009. And these solutions have been corrected with respect to ellipsoidal earth (*Ditmar, 2018*) and these corrections are carried out separately for land and ocean so as to prevent leakage in signals. Mascons parameters are basically geodesic tile elements which are used in estimation of mass correction globally to a priori mean background model, and the mass variability is expressed in centimetre of equivalent water height (uniform water mass layer). The mascon formulation has been expressed by the analytical expression given by (*Rowlands et al., 2010*) (Eq. (1)):

$$H_j(\vartheta\lambda\, t) = \left[\frac{M}{40\pi R^2}\right] * \sum_{l=0}^{\infty} \frac{2l+1}{1+k_l} \times \\ \times \sum_{m=0}^{l} \overline{P_{lm}}\ (\sin\vartheta) * [\Delta C_{jlm} \cos m\lambda + \Delta S_{jlm} \sin m\lambda]\ , \tag{3}$$

where, $H_j(\vartheta\lambda\, t)$ is the mascon parameter of the j-th region at time, t, and it is a scalar, ϑ is the latitude, λ is the longitude, M is the Earth's mass, R is the mean radius of the Earth, l and m represent the spherical harmonic degree and order, $\overline{P_{lm}}$ represent the fully normalized associated Legendre functions, ΔC_{jlm} and ΔS_{jlm} are change in change in potential coefficients.

The change in potential coefficients (ΔC_{jlm} and ΔS_{jlm}) is explained as addition of small uniform layer of mass over a region. This uniform mass

layer is considered as geodesic tile which is represented as j in the potential coefficient change. The detailed steps of processing have been explained in (*Save et al., 2016*). Also, the mascon solutions are derived only from GRACE satellite and not from any external geophysical data or model. Although the native resolution of the data is $1^\circ \times 1^\circ$ but for the ease of analysis and diversified use these data are resampled into $0.25^\circ \times 0.25^\circ$.

In this study we have used GRACE & GRACE-FO satellite's CSR RL06 mascon solutions ($0.25^\circ \times 0.25^\circ$) that are obtained from `http://www2.csr.utexas.edu/grace`. The Terrestrial Water Storage or TWS is estimated by GRACE comprising both soil moisture and groundwater. GLDAS (0.5°) NOAH (2.1) uses a monthly dataset to calculate the Total Water Content (Soil Moisture, Snow Water equivalent, Surface Water Runoff etc.). Subsequently, the GWS/GWSA is calculated using the Eqs. (4) & (5) (*Gautam et al., 2017; Karunakalage et al., 2021*):

$$\Delta\mathrm{GLDAS}_{\mathrm{Total}} = [(\mathrm{TSM} + \mathrm{CWS} + \mathrm{SWE}) - \mathrm{Mean}(\mathrm{TSM} + \mathrm{CWS} + \mathrm{SWE})], \tag{4}$$

$$\Delta\mathrm{GWS} = \Delta\mathrm{TWS} - \Delta\mathrm{GLDAS}_{\mathrm{Total}}\,. \tag{5}$$

GRACE provides the vertical change (detected by the change in separation distance between the twin satellite) in mass on Earth's surface, which can vary per grid of the dataset. Thus the GWS change or the groundwater fluctuation is estimated per pixel/grid in the seven basins from 2002–2020 to get an idea of change in GWS rate over the year for each dataset (CSR-M, JPL-M, SH) by using the Eq. (6).

$$\Delta\mathrm{GWS}^{\mathrm{grid}}_{\mathrm{mass}} = \frac{\mathrm{array}^{N}_{i=1}(\Delta\mathrm{GWS}^{\mathrm{grid}}_{\mathrm{flux}_i})}{\sum\limits_{i=1}^{N} \mathrm{Time\ Period}} \times \mathrm{Pixel\ Area}\,. \tag{6}$$

[N is the number of years in the studied period, and i is the respective year].

For developing the 2D GWS maps, we have used Kernel interpolation with barriers. This method is similar to polynomial interpolation, which can easily detect obstacles in the study area. It even allows accurate checking of contamination levels in lakes compared to the other methods used for adjusting barriers (*Sarkar et al., 2020*). We have created 2D GWS mass loss maps to study long term mass change in the seven basins (Figs. 7, 8).

3.3. Decomposition of seasonal components from GWSA time series using the STL-LOESS regression approach

The GWS time series (estimated grid wise) requires removal of the seasonal components after the missing data gaps are filled, which is done by Linear Interpolation method using months of either side with respect to no data month (Eqs. (6) & (7)) (*Andrew et al., 2017; Neves et al., 2020*).

$$\frac{\Delta \mathrm{TWC}_t}{\mathrm{grid}^{i^0}} = \frac{1}{\mathrm{grid}^{i^0}} \sum \Delta \mathrm{SM}_t + \Delta \mathrm{CW}_t + \Delta \mathrm{SW}_t \,, \tag{7}$$

[i^0 is spatial resolution in degree, t is temporal resolution in months, ΔSM, ΔCW, and ΔSW are monthly changes in soil moisture, canopy water and snow water with respect to time mean baseline of 2004–2009],

$$\frac{\Delta \mathrm{GWS}_t}{\mathrm{grid}^{i^0}} = \frac{1}{\mathrm{grid}^{i^0}} (\Delta \mathrm{TWS}_t - \Delta \mathrm{TWC}_t) \,. \tag{8}$$

The Seasonal Trend decomposition (STL) approach shows analogous results with harmonic analysis, which is sturdy and compliant for decomposing the GWSA time series (Fig. 4), estimated by the Eq. (9):

$$\begin{aligned} {}^{t}_{\mathrm{grid}}\Delta \mathrm{GWS}_{\mathrm{total}} = {}^{t}_{\mathrm{grid}}\Delta \mathrm{GWS}_{\text{long-term}} + {}^{t}_{\mathrm{grid}}\Delta \mathrm{GWS}_{\mathrm{annual}} + \\ + {}^{t}_{\mathrm{grid}}\Delta \mathrm{GWS}_{\text{semi-annual}} + {}^{t}_{\mathrm{grid}}\Delta \mathrm{GWS}_{\mathrm{residual}} \,, \end{aligned} \tag{9}$$

[t is the seasonal window].

In this study, we use Seasonal Trend Decomposition (STL) approach (*Cleveland et al., 1990; Hafen, 2016*) using LOESS smoothening, which is a polynomial fitting, generated by a smoothed series as $X(j)$ fit with the time window derived input time series as $X(j) = X(t_j)$, where, t_j is an array of the sampling window. Each value of smoothed time series is given by the value that has been derived by t_j of the derived fitted polynomial curve of the sampling values of X over the time window as $(j-q,\ j+q)$, which has determined decreasing weighted value according to the distance to point X from q. We have used 12 months window here because it helps remove all small level disturbances (*Khorasani et al., 2016*). The three decomposed components are $\mathrm{GWS}_{\text{long-term}}$ (linear and non-linear trends/interannual variability), $\mathrm{GWS}_{\mathrm{seasonal}}$ (seasonal variation or short-term trend) and Residuals (noise, signals and sub-seasonal change). Residuals are mainly the local phenomenon or effects that lead to variability in the groundwater system. At

the same time, GWS_{long} is determined by mid to long period climatic oscillation, and the $GWS_{seasonal}$ indicates cyclic phenomena like El-Nino effects affecting the groundwater system (*Lafare et al., 2016*). The residuals are estimated after subtracting the other components from GWS_{total} equation (where interannual and subseasonal signals might be present). The need to remove residuals and short-term trends is to perceive a clear idea about the long-term fluctuation of groundwater in an aquifer. As we know, groundwater recharge or water percolation from surface to subsurface is quite a time-consuming phenomenon. So, the water within the vadose zone (presumed as seasonal and sub-seasonal components) is subtracted or removed to estimate the long-term GWS in the water table (Figs. 4 & 5, Table 1).

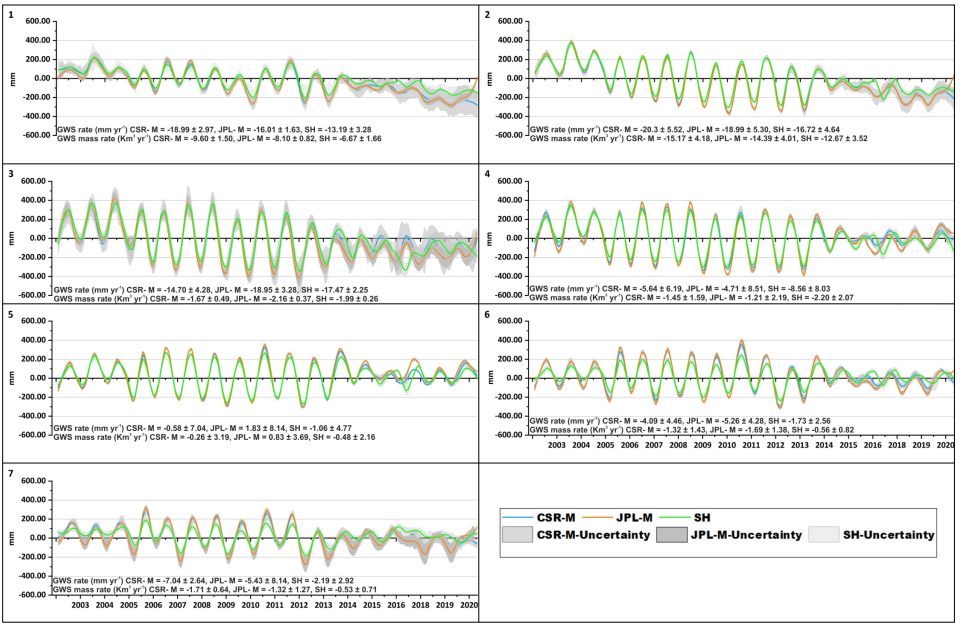

Fig. 4. GWS decomposed time series showing long term trend, in respect to GWS rate (mm/yr) and GWS mass rate (km^3/yr), along with its uncertainties (basin wise, 95% confidence level) is observed in all the river basins (Basin 1–7) from 2002–2020.

3.4. Grid wise and Basin wise GWS Uncertainty estimation

The uncertainty estimated for GWS is done in two ways with annual basin and per grid error of 95% confidence by the distribution of 20 years average

Table 2. Basin wise (1–7) Uncertainty (for GWS rate and GWS mass rate) estimated with 95% confidence level in each basin and for the three GRACE datasets.

Basin Number	Error for GWS rate			Error for GWS Mass rate		
	CSR±	JPL±	SH±	CSR-M±	JPL-M±	SH±
1	2.97	1.63	3.28	1.50	0.82	1.66
2	5.52	5.30	4.64	4.18	4.01	3.52
3	4.28	3.28	2.25	0.49	0.37	0.26
4	6.19	8.51	8.03	1.59	2.19	2.07
5	7.04	8.14	4.77	3.19	3.69	2.16
6	4.46	4.28	2.56	1.43	1.38	0.82
7	2.64	5.23	2.92	0.64	1.27	0.71

values (Table 2). Each grid is weighted by averaging its area while counting its contribution to the histogram (grid value points and its probability function distribution in these 20 years) for adjusting the distribution value from high to low latitude (*Wahr et al., 2006*).

In the case of basin wise uncertainties (suggested by *Scanlon et al., 2016*) we have carried out uncertainty appraisal in all seven basins for each dataset (CSR-M, JPL-M and SH). The CSR-M data uncertainty is calculated after the GWS time series decomposition Eq. (8). It is estimated from the residuals after long-term trends, and seasonal trends are removed (*Scanlon et al., 2016*). However, these uncertainties might overestimate the actual uncertainty due to noise and signal present in the residual component. In JPL-M data, both leakage and measurement errors are taken into consideration. The measurement errors are already available on the website. They are exhibited in the form of formal measurement by applying scaling factor 2 (*Wahr et al., 2006*). The leakage errors are calculated by synthetic simulation for the seven basins (*Wiese et al., 2016*). Finally, in SH data, the measurement errors of GRACE Level 1 are included in the Level 3 monthly solutions (considered in this study) along with the leakage error (which is the difference between GWSA (calculated from GLDAS)) and GWSA (with scaling factors) (*Landerer and Swenson, 2012*).

Pixel base standard deviations are derived for GRACE & GLDAS, and the final uncertainty error is calculated with first-order error propagation using Eq. (10). After that, it is compared with GRACE-GLDAS derived

GWS by using the Eq. (11). Pixel Wise uncertainty estimation is carried out per pixel/grid for the three datasets (CSR-M, JPL-M and SH) from 2002–2020 using filtered pre-processed TWS and TWC (Total Water Content) (*Karunakalage et al., 2021*) using Eq. (12):

$$Z = a\,X \pm b\,Y\,, \tag{10}$$

$$\sigma Z = \sqrt{a^2 \cdot \sigma^2 X + b^2 \cdot \sigma^2 Y}\,, \tag{11}$$

[a and b are scalar constants and σX and σY are standard deviations of uncorrelated components].

From equations (10) and (11), we finally derive the uncertainty per grid, and all these results correlate with *Boergens et al. (2020)*:

$$\text{Uncertainity}_t^{\text{grid}} = \frac{1}{N}\sqrt{\sigma_t^2\,\text{TWS} + \sigma_t^2\,\text{TWC}}\,, \tag{12}$$

[t is one month period, and N is the number of pixels in the basin]. The uncertainties estimated at the basin wise scale are less than grid wise calculations (*Scanlon et al., 2016*).

3.5. Estimation of deseasonalized GWS mass loss

The study area is classified into seven river basins; in this classification, Basin 1,2,3 encompasses Northern India and are glacier melts from the Himalaya. At the same time, the remaining river basins (4–7) flow over the Indian Peninsular shield. We have estimated the groundwater mass loss for each basin (from the 2D groundwater mass loss map) by extracting its respective area. In this study, we have estimated the GWS mass loss for two decades i.e. 2002–2020 (Fig. 8).

3.6. Estimation of vertical deformation from GPS data and its correlation with GWS

The GPS data from IGS (International GNSS Service) stations Lucknow, and IISC Bangalore has been processed in GAMIT/GLOBK 10.71 software with respect to ITRF2014 from January 2017 – December 2020, giving daily solutions, showing variation both in the horizontal and vertical component. The results have been consistent with certain previous studies like *Sneed et*

al. (2001); Sahu and Sikdar (2011); Choudhury et al. (2018); Ojha et al. (2019).

For this study, we considered the Vertical deformation and then correlated it with GRACE derived GWS change and estimated Linear regression (R^2) and Correlation Coefficient (ρ) between them for getting a clear picture about the groundwater variation in active tectonic regions (Fig. S4) (*Machiwal et al., 2011; Yadav et al., 2021; Kannaujiya et al., 2022*).

3.7. Land deformation/subsidence study using SAR and its relation with GWS

- **SAR data processing**

  We downloaded pre-monsoon images of the 2016–2020 period from the Alaskan Search Facility, using Sentinel 1A C band (5.05 GHz) in Interferometric Wide Swath Mode along the descending track. The further processing step is carried out in GMTSAR using the SBAS technique in the cities where the GWSA rate shows negative trends fatally. It is done to validate the development of any land subsidence or surface deformation caused by excessive groundwater pumping. The area of interest includes certain Indian cities (Chandigarh, New Delhi, Mehsana, Lucknow, Kolkata, Bengaluru) through which the selected seven basins flows along with population hike and industrialization (Figs. 1, S6). A total of 39 tiles have been processed from the images for these six cities. The processing of SAR data needs orbit files downloaded from the ESA (European Space Agency) portal. In the two-pass DInSAR technique, SRTM-DEM (30 m resolution) in 'grd' format removes the phase difference caused by phase topography. The data product used for Interferometry processing is in SLC format.

  A certain number of images are selected to develop time series for precise analysis of land deformation. After that, all the XML and TIFF files are stacked in one location at three interferometric sub swaths (iW1, iW2, iW3), and plotted the perpendicular baselines vs time, which is the pre-processing step in GMTSAR, the already downloaded orbit files have detailed information about the position and updated metadata of the SAR image. These stacked images are aligned and co-registered using the command *pre_proc_batch_tops.csh data.in dem.grd 1.*

The filename extension with data.in is the file for images and orbit files. From the baseline vs time plot, a super master image is selected so that it lies in the middle of the plot. The super master image is saved under 'data.in' filename. So, taking it as a reference, all the previously stacked saved DEM and other images are coregistered using the command *pre_proc_batch_tops.csh data.in dem.grd 2*, which further helps in generating interferograms (Fig. S5a-f).

- **Interferogram generation**

  A pair is selected for which interferogram generation is to be done. The selection of pairs is made within threshold limit in baseline plot with respect to Super master image using the command *select_pairs.csh baseline _table.dat 50 100* and are saved under 'intf.in' file name (Threshold limit in SBAS is 50 days and 100 m). After selecting pairs is completed, the following command is used for modifying the 'batch_tops.config' file where the master image is determined along with filter wavelength, range decimation, azimuth decimation values, snaphu threshold and geodetic threshold. *intf_tops_parallel.csh intf.in batch_tops.config*. All the processing is carried out at different subswaths, so the swaths need to be merged using the command *merge_batch.csh merge_list batch_tops.config*.

- **Unwrapping of Interferograms**

  After merging the subswaths, the interferogram is unwrapped by considering the wrapped phase image intensity, interferogram coherence and topographic phase (derived from external DEM) (*Berardino et al., 2002; Rosen, 2000*). It is done by using the command *unwrap_parallel.csh intflist*.

- **Application of SBAS (Short BAseline Subset) technique**

  SBAS (Short BAseline Subset) technique estimates vertical velocity and studies the land surface deformation evolved over time. It is identified by a small baseline separation between the two SAR images used for interferogram generation. It also detects large scale displacement with comparatively low resolution. The input files are created for SBAS analysis; one is intf.tab, which comprises list of paths to unwrapped interferogram (unwrap.grd), correlation grid (corr.grd), reference scene id, secondary

scene id and difference in the perpendicular baseline. Whereas, the other input file is scene.tab which contains scene ids and the number of days. The GMTSAR command applied for this analysis is:

sbas intf.tabscene.NS xdim ydim[-smooth sf][-wavelength wl][-incidence inc][-range rng][-rms][-dem]

N = Number of interferograms, S = Number of scenes, *xdim* = no. of columns in the interferogram, *ydim* = no. of rows in the interferogram, *sf* = smoothening factor, *wavelength* = 0.0554658 for C-band, incidence = 40 degrees, average incidence angle for TOPS acquisition, *range* = ({[(speed of light) / (*rng_samp_rate*) / 2] * ((*x_min*+*x_max*)/2)}/2) + *near_range*.

The groundwater mass rate values obtained from the 2D groundwater mass rate map relies on differential interferograms derived velocities by pixel image correlation. Therefore, both layers are made on the same pixel size by resampling. The correlation procedure only targets that area where deformation fringes lie over the respective city. First, the target area is extracted from both the groundwater mass rate map and the deformation layer of DInSAR. Then the covariance image has been generated based on Eq. (13):

$$\text{Covariance}_{kl} = \sum_{i=1}^{N} \frac{(Z_{ki} - \bar{Z}_k)(Z_{li} - \bar{Z}_l)}{(N-1)}, \tag{13}$$

[k and l are Mass rate map layer and DInSAR velocity map layer, Z_i is the value of the pixel, and $\bar{Z}$ is the average pixel value of the layer].

The covariance image is further converted to the correlation image by the Eq. (14):

$$\text{Correlation}_{kl} = \sum_{i=1}^{N} \frac{\text{Covariance}_{kl}}{\sigma_k . \sigma_l}, \tag{14}$$

[σ is the standard deviation of the layer].

The positively correlated pixels have been extracted (PCA). After that, the area from the layers is re-extracted by using these PCA as a mask. The re-extracted images are used to generate the correlation image between

maximum groundwater mass change and vertical deformation velocity at the PCA (Fig. S6).

4. Results

4.1. The regional behavioural change in SPI inferred from CHIRPS

Sudden climate change has miserably disturbed the seasonal rainfall pattern leading to escalated drought conditions. Over the years, the drought condition has increased or decreased, transforming many areas from semi-arid to arid. To monitor and evaluate the historical droughts, we employed a 6-month scale SPI or Standardized Precipitation Index to determine the rainfall change in selected seven river basins from 2002–2020. The averaged SPI values (blue curve) calculated using CHIRPS is shown in Fig. 2a. The SPI values for all the seven basins lie within ~ 0 to (+) 2 range and characterizes drought into different categories like; Normal (green), moderate (yellow), severe (light orange) and extreme (brown) (Fig. 2a), thus justifying the Tom McKee's classification (already discussed in Section 3.2). In the initial years, 'i.e.', from 2002–2004, we can see a rise in extreme drought condition (highlighted in dark brown peak) covering almost an area of 80% in Basin 1, wherein the remaining six basins too witness the same drought condition but in a small spatial extent of $< 40\%$.

Consequently, down the line, the drought intensity in all the seven basins starts to normalize, and a greater spatial area ($> 80\%$) is covered with green colour, which means Normal or wet conditions. However, sporadic brown and light orange patches prevail with an exception at Basin 7 in 2017–2018, where extreme drought condition (brown peak) has almost engulfed 80% of the spatial extent. Therefore, we can infer that rainfall took a thriving comparative turn in 2005–2020 in all the basins.

4.2. Seasonal GWS change with pixel-based uncertainty and its relation with the SPI change

The Earth have a solid crust and viscoelastic mantle, in this context, elastic deformation takes place when the hydrological loading increases in co-monsoon and post-monsoon months (November & December). On the contrary, elastic rebound occurs during post-monsoon unloading (January &

February) and pre-monsoon time (*Kannaujiya et al., 2021*). The GWS change estimated per grid (CSR-M, JPL-M, SH) carried out in seven basins (that belongs to both Himalayan & Peninsular River system) gives a clear idea regarding the groundwater use or misuse happening India. GWS change for every year (2002–2020) is observed with respect to pre (March–July), co (August–October) and post (November–February) months (Fig. 3). The interannual GWS depletion in all river basins improves in co monsoon and post-monsoon (Nov–Dec) but shows a drastic transformation (bowl-shaped depression curve) in post-monsoon (Jan–Feb) and pre-monsoon months, thereby exhibiting a sinusoidal curve. During the post-monsoon (Jan–Feb) and pre-monsoon months, the GWS depletion value reaches −150 mm/yr. Consequently, GWS escalates and comes within a value range of ∼50 to 150 mm/yr in co and post-monsoon months (November and December). Now, comparing the results of GWS (mm/grid) with SPI (Fig. 2b), it has been observed that from 2005 onwards, the SPI index improves and indicates low drought intensity, but on the contrary, GWS reacts adversely. The GWS estimated per grid for the 2002–2020 period from CSR-M, JPL-M and SH datasets shows an alarming rate of GWS depletion in Basin 1–4. The GWS trends with its uncertainty is estimated and the values are: for basin 1, -18.9 ± 1.42 (CSR-M), -16.09 ± 1.55 (JPL) and -17.52 ± 1.65 (SH); for basin 2, -20.10 ± 1.81 (CSR-M), -19.0 ± 2.02 (JPL-M) and -16.09 ± 1.68 (SH); for basin 3, -18.94 ± 1.2 (CSR-M), -16.09 ± 1.55 (JPL-M) and -17.52 ± 1.65 (SH); for basin 4, -5.79 ± 0.66 (CSR-M), -4.86 ± 1.01 (JPL-M) and -8.60 ± 0.52 (SH).

In contrast to this the GWS trend values with its uncertainty for basin 5, 6 and 7 are as follows: for basin 5, -0.75 ± 0.47 (CSR-M), -1.62 ± 0.60 (JPL-M) and -1.12 ± 0.32 (SH); for basin 6, -4.24 ± 0.60 (CSR-M), -5.39 ± 0.67 (JPL-M) and -1.70 ± 0.38 (SH); for basin 7, -7.11 ± 0.64 (CSR-M), -5.47 ± 0.36 (JPL-M) and -1.97 ± 0.36 (SH). Therefore, we can infer from these trend values that the Northern and a part of the Central region of India are comparatively facing a dire water crisis.

4.3. Inference from GWS estimation with basin wise uncertainties

We have calculated GWS uncertainty in terms of rate and mass rate, and the results are mentioned in Table 1 with a 95% confidence level (Table 2). The GWS trends with its basin wise uncertainty is estimated and the val-

ues are: for basin 1, -18.9 ± 2.97 (CSR-M), -16.01 ± 1.63 (JPL) and -13.19 ± 3.28 (SH); for basin 2, -20.3 ± 5.52 (CSR-M), -18.99 ± 5.30 (JPL-M) and -16.72 ± 4.64 (SH); for basin 3, -14.70 ± 4.28 (CSR-M), -18.95 ± 3.28 (JPL-M) and -17.47 ± 2.25 (SH); for basin 4, -5.64 ± 6.19 (CSR-M), -4.71 ± 8.51 (JPL-M) and -8.56 ± 8.05 (SH). On the other hand, the contrasting GWS rate for basins 5–7 is as follows. For basin 5, -0.58 ± 7.04 (CSR-M), 1.83 ± 8.14 (JPL-M) and -1.06 ± 4.77 (SH); for basin 6, -7.11 ± 0.64 (CSR-M), -5.47 ± 0.36 (JPL-M) and -1.97 ± 0.36 (SH); for basin 7, -7.04 ± 2.64 (CSR-M), -5.43 ± 8.14 (JPL-M) and -2.19 ± 2.92 (SH). GWS mass rate (km^3/yr) lie in range of -15.17 ± 4.18 to -1.67 ± 0.49 for basins 1-3 and differs by -1.71 ± 0.64 to -0.26 ± 3.19 km^3/yr for basins 4–7 (Fig. 4). The JPL-M and SH datasets are compared with CSR-M because it has the highest grid resolution and is also not required for post-processing. Therefore, we formed scatter plots for understanding the relation among the three GRACE & GRACE-FO datasets with respect to CSR-M and then calculated ρ (correlation coefficient) and r^2 (linear regression). The results (Table 1) from scatter plots are characterized according to the basin wise spatial extent as large (> 400000 km^2), medium (≥ 200000 km^2) and small ($10000 \leq \text{area} \leq 200000$ km^2).

4.4. Implication of variation in the long term (mm/yr) and short term (mm/month) groundwater storage in terms of rate (mm/yr) and mass rate (km³/yr)

The deseasonalization from Eq. (8) includes both long-term and short-term trends, estimating the GWS rate and the GWS mass rate (Table 1 & Fig. 4). The long-term trend shows depleting GWS rate values upto ~ -20 mm/yr for Basin 1, 2, 3 and ~ -4 to ~ -7 mm/yr for basins 6, 7, 5. We have already differentiated basin 5 under the large category and 3 under the small basin category, but despite their spatial extent, their GWS rate varies adversely. Similar results are perceived in short term trend GWS rate. In long term trends, the value of mass is depleting in basins 1 and 2, corresponding to the GWS rate. The GWS mass rate observed in basin 4, 5, 6, 7 is almost equivalent to the GWS rate. But the GWS mass rate increases in basin 3 and behaves adversely to the GWS rate. Similar results are estimated from short term trend too. From our analysis, we can infer that basin 1, 2 ,3 (includes Ganga, Brahmaputra and some west-flowing rivers), which covers

mostly the Northern regions of India, has a high GWS rate and mass rate. *Scanlon et al. (2016)* have also estimated high GWS rate and mass trends (both long and short term) at Ganga-Brahmaputra rivers and basins where irrigation is maximum.

4.5. The idea of removing residuals and why?

Residuals are mainly local phenomena that affect the groundwater system or the presence of surface water in the vadose zone, which takes time to reach the water table, is treated as noise or disturbance and thus needs to be removed. The residuals in all seven basins (Fig. S3) are estimated from 2002–2020 after applying STL decomposition on GWSA time series (where seasonal component is embedded) using CSR-M (Fig. S3a), JPL-M (Fig. S3b) and SH (Fig. S3c). The averaged final estimates are shown in Fig. 5 as Residual Positive Amplitude (RPA) and Residual negative Amplitude (RNA) for CSR-M (blue), JPL-M (orange) and SH (green) datasets.

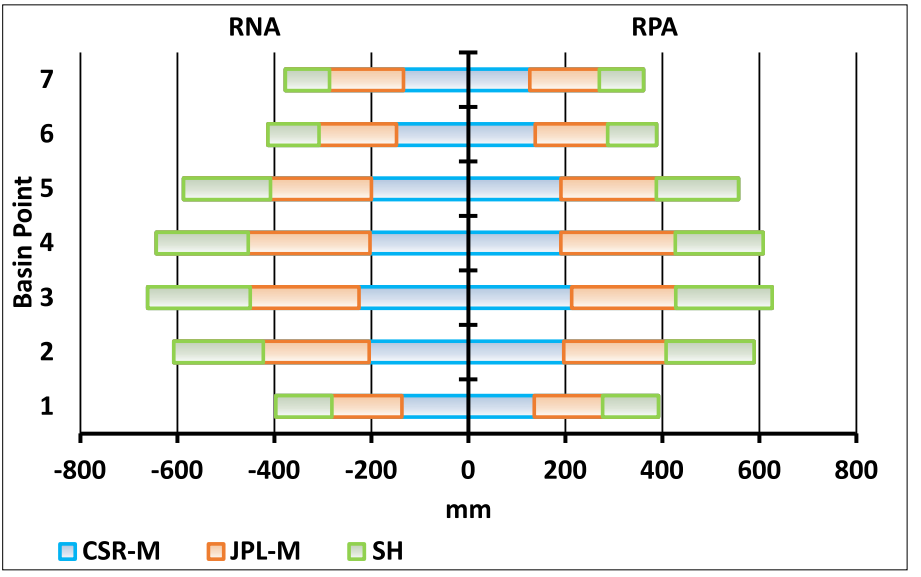

Fig. 5. The RPA (Residual Positive Amplitude) and RNA (Residual Negative Amplitude) residuals estimated after applying (STL) Seasonal Trend decomposition on GWS time series (where seasonal component is embedded) shown by CSR-M, JPL-M and SH datasets for all the seven river basins (Basin 1–7).

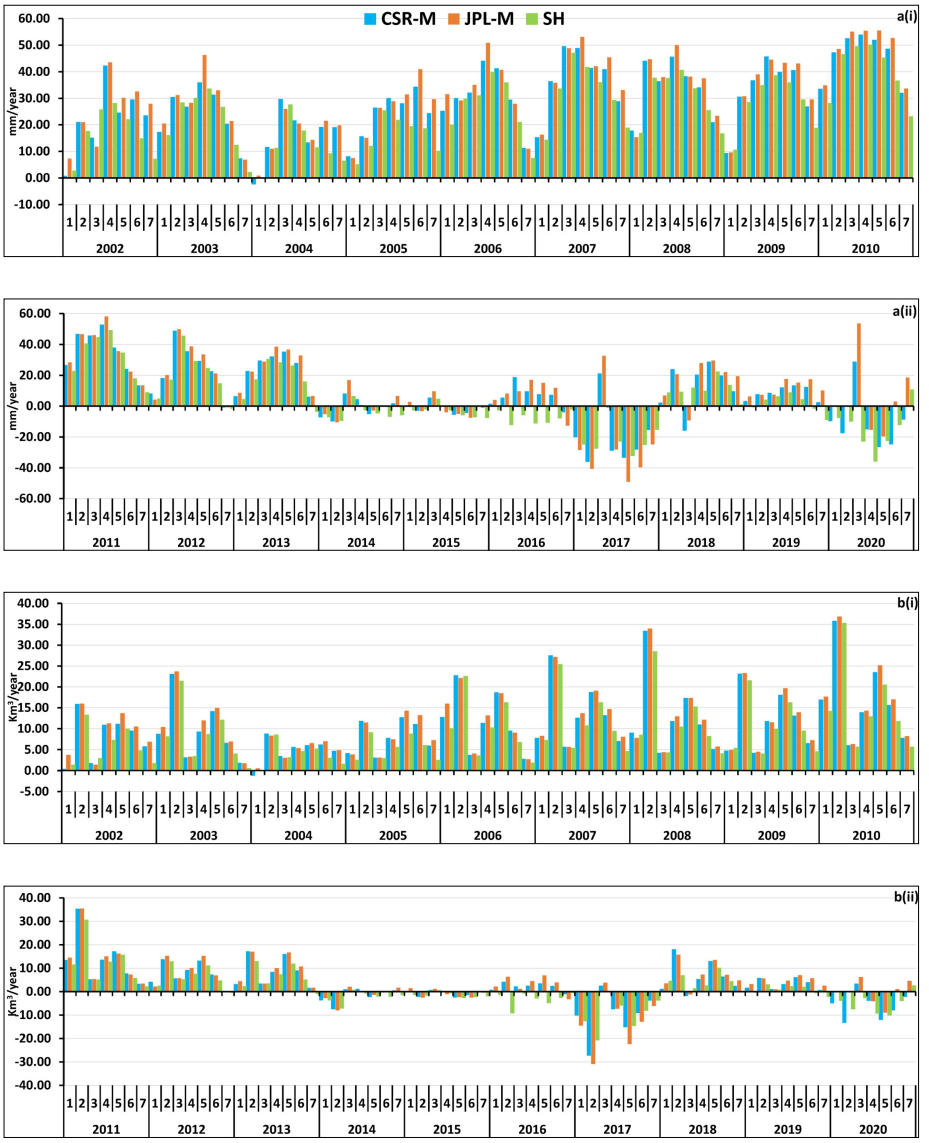

Fig. 6. The variation in (a(i)) GWS rate (mm/yr) for 2002–2010 (a(ii)) GWS rate (mm/yr) for 2011–2020 and (b(i)) GWS mass rate (km^3/yr) for 2002–2010 and (b(ii)) GWS mass rate (km^3/yr) for 2011–2020, estimated in all the seven basins after deseasonalization carried out by Seasonal Trend (LOESS Regression) decomposition approach.

In the case of both RPA and RNA, the values of JPL-M exceed slightly, unlike CSR-M and SH. It is observed that basin 3 have high residual values compared to the large basins 1, 2, 5. Therefore, it can be inferred that residual variations don't depend on the spatial extent of a basin (*Scanlon et al., 2016*).

4.6. Inferences from Seasonal Trend decomposition approach

The decomposition of the GWSA time series using Eq. (8) for the seven basins is shown in Fig. S2a-c & Fig. 6. After removing the seasonal components, the deseasonalized GWS rate (estimated annually) shows positive values till 2010. But the situation changed after 2010 when GWS rates started showing negative value by the end of 2014 (~ -10 mm/yr) and continued to decrease to a rate of ~ -40 mm/yr. In 2018–2019 the GWS rate improved (except for basins 1, 2) but started to fall again in 2020 (Fig. 6a&b). Consequently, the deseasonalized GWS mass rate maintained a positive value until 2013 (~ 35 km^3/yr) but changed after 2014 (~ -30 km^3/yr). The GWS mass rate becomes negative and continues to be the same, slightly improving in 2019. Thus, the situation worsens mainly from 2014 and affects mostly basin 1, 2.

4.7. Inference from deseasonalized GWS mass loss estimation in and around the Indian River basins

Considering the seven river basins, deseasonalized GWS mass loss (2002–2020) has been estimated (with respect to its spatial extent) to substantiate the immense groundwater depletion in the country. The estimation states that Himalayan River basins 1,2,3 exhibit high GWS mass loss (-260 to -35.12 km^3), with Basin 2 being the highest (-260 km^3). Whereas the Peninsular River basin 4,6,7 gives moderate mass loss value from -26.72 to -23.58 km^3. And in River basin 5, the GWS mass loss observed is the lowest, with a value of -8 km^3.

4.8. Effects of ground deformation due to groundwater storage variations in respect to GPS

The vertical displacement of IGS stations LCK3 and IISC is estimated as -2.18 ± 0.27 mm/yr and -1.86 ± 0.22 mm/yr, respectively, from 2017–2020.

After correlating the GPS vertical displacement from these two stations with GWS change, we observe positive Linear regression and negative correlation coefficient. The Linear regression for LCK3 is 0.34 (CSR-M), 0.40 (JPL-M) and 0.07 (SH) and for IISC is 0.009 (CSR-M), 0.001 (JPL-M) and 0.01 (SH). Correlation between the GPS and GRACE change is negative with values $-0.89-(-)0.54$ (CSR-M), $-0.96-(-)0.45$ (JPL-M) & $-0.90-(-)0.21$ (SH) for IISC and $-0.7-(-)0.48$ (CSR-M), $-0.71-(-)0.41$ (JPL-M) & $-0.66-0.11$(SH) (Table 3).

Table 3. Linear Regression and correlation calculated between GPS and GWS change to study the associated effects of ground deformation.

Linear regression between GRACE GWS and GPS			
Component	Solution	City	
		IISC (Bengaluru)	LCK3 (Lucknow)
r^2	CSR-M	0.34	0.009
	JPL-M	0.40	0.001
	SH	0.07	0.01
Correlation between GRACE GWS and GPS			
Year	Solution	IISC (Bengaluru)	LCK3 (Lucknow)
2017	CSR-M	−0.51	−0.40
	JPL-M	−0.48	−0.64
	SH	−0.21	−0.50
2018	CSR-M	−0.82	−0.41
	JPL-M	−0.91	−0.63
	SH	−0.85	−0.27
2019	CSR-M	−0.89	−0.37
	JPL-M	−0.90	0.16
	SH	0.18	0.11
2020	CSR-M	−0.54	−0.70
	JPL-M	−0.96	0.71
	SH	0.73	0.66

4.9. Effects of ground deformation due to groundwater storage variations in respect to SAR

SBAS gives the LOS (Line of Sight) displacement velocity in the six prominent cities of India (Chandigarh, Delhi, Lucknow, Mehsana, Kolkata and

Bengaluru) from 2016 to 2020. The sky blue colour from the histogram bar indicates the individual maximum vertical velocity for each city. In Chandigarh, the deformation hotspot (sky blue colour) showing −113 mm/yr vertical velocity is located in the Northwest, continuing towards the Southeast direction (Fig. 10a). The deformation spot in Delhi is located centrally and vary from sky blue (−26 mm/yr) to light green colour (Fig. 10b). Unlike Delhi and Chandigarh, the deformation zone in Mehsana is present in patches covering the entire Mehsana region with vertical velocity −63 mm/yr (Fig. 10c). Moving on to Lucknow, the deformation spots are scanty and cover significantly less area with vertical velocity −22 mm/yr (Fig. 10d). Treading towards the Eastern part of India, we come across Kolkata, where the deformation zone covers quite a large area, mainly in the Southwestern part showing vertical velocity −95 mm/yr (Fig. 10e). Consequently, after shifting to South Indian city Bengaluru, the deformation hotspot occurs sporadically with vertical velocity −33 mm/yr (Fig. 10f). All our observations are supported to an extent by studies of eminent researchers (*Ittycheria et al., 2018; Suganthi and Elango, 2020; Garg et al., 2020*).

Next, we carried out correlation measurements between SAR data and GWS mass rate (Table 4 & Fig. S6) and aptly quantified the ground deformation effects (*Castellazzi et al., 2016*). We observed a positive correlation, and the values are 0.20, 0.07, 0.06, 0.08, 0.53 and 0.27 in Chandigarh, Delhi, Mehsana, Lucknow, Kolkata and Bengaluru, respectively. The positive correlation area is 55.3% in Chandigarh, 48.7% in Delhi, 66.65% in Mehsana, 54% in Lucknow, 72.7% in Kolkata and 61% in Bengaluru, out of total cor-

Table 4. Correlation coefficient study carried out between Sentinel 1A SAR and GWS mass rate evaluated the GWS mass rate with respect to maximum vertical displacement (observed in the positively correlated area).

Component	**City Name**					
	Chandigarh	New Delhi	Mehsana	Lucknow	Kolkata	Bengaluru
Total Correlation	0.20	0.07	0.06	0.08	0.53	0.27
Correlated Area	3291	675	145	420	1902	382
Positive Correlation	55.3	48.7	66.65	54.00	72.70	61.00
Max VD in PCA	−69.69	−25.73	−62.19	−15.01	−94.35	−32.16
Max GWS Mass	−0.009	−0.0085	−0.0005	−0.0019	−0.0013	−0.001

related area 3291 km^2, 675 km^2, 145 km^2, 420 km^2, 1902 km^2, 382 km^2 respectively. Maximum vertical velocity observed in this positively correlated area is high in Kolkata and lowest in Lucknow. But in contrast to that, the GWS mass rate is high (-0.0085 km^3/yr) in Delhi, with Kolkata (-0.0013 km^3/yr) ranks third after Lucknow (Table 4).

5. Discussion

The relation between SPI and GWS revealed the bitter truth about groundwater exploitation, especially in North Indian regions. So, we delved deeper and found out that population rise is the main reason behind groundwater exploitation. In this context, we estimated the correlation coefficient (ρ), and Linear regression (R^2) between GWSA and the area used up for irrigation (Fig. S7) in seven basins. Along with that, we also checked the population hike and urbanization rise from 2008–2014. For basins 1 and 2, there is a tremendous increase in population compared to the other five basins. The correlation between GWS and the irrigational area is positive for all the seven basins, which means an increase in irrigation (due to population hike) leads to a rise in GWS depletion. Accordingly, the linear regression is positive for basins 1–3, indicating a rise in population led to rising in irrigational areas and depletion of GWS. While the basin 4–7 show negative linear regression, 'i.e.', even after rise in population the irrigational land use is controlled along with the GWS change. To substantiate the groundwater fluctuation in all the seven basins, we analysed how much area (per grid) is affected by variation in groundwater storage (mm/yr) in 2002–2007, 2008–2013 and 2014–2020 (Fig. 9). All significant fluctuations or changes have started after 2014. The Basin 1, 2, 3 or Northern basins show depleting GWS rate (~ -150 to -100 mm/yr range) is covering a maximum percentage of the area ($\sim 30-80\%$), whereas the Basin 4–7 shows that maximum percentage aerial extent ($\sim 90\%$) is covered by positive GWS rate ($\sim 0-50$ mm/yr) (Table S2a-g). This paradox can arise as GRACE & GRACE-FO data fails to determine changes at a local scale because the data is aggregated on a larger scale. The other reason could be the heterogeneous aquifer distribution found in these regions (*Hora et al., 2019*).

The deseasonalized GWS mass rate (per grid) observed in Basin 1–7 are studied in six respective cities (Chandigarh, Delhi, Mehsana, Lucknow, Kolkata and Bengaluru) in relation to Precipitation and change in GWS rate taking place here (Fig. 7g). In Chandigarh, the GWS mass rate is depleting (~ -0.009 km^3/yr) along with its GWS rate (Fig. 7a) despite receiving $\sim 300-500$ mm rainfall. Likewise in Delhi receives $\sim 400-200$ mm rainfall and face depletion in GWS mass rate (~ -0.009 km^3/yr) & GWS rate (Fig. 7b). The rainfall received in Lucknow is quite thriving $\sim 400-500$ mm with a moderately low GWS mass rate and highly depleting GWS rate (Fig. 7c). In Mehsana, the GWS mass rate is around ~ 0.0006 km^3/yr, with a rainfall of $\sim$ 450 mm and moderate depletion of the GWS rate

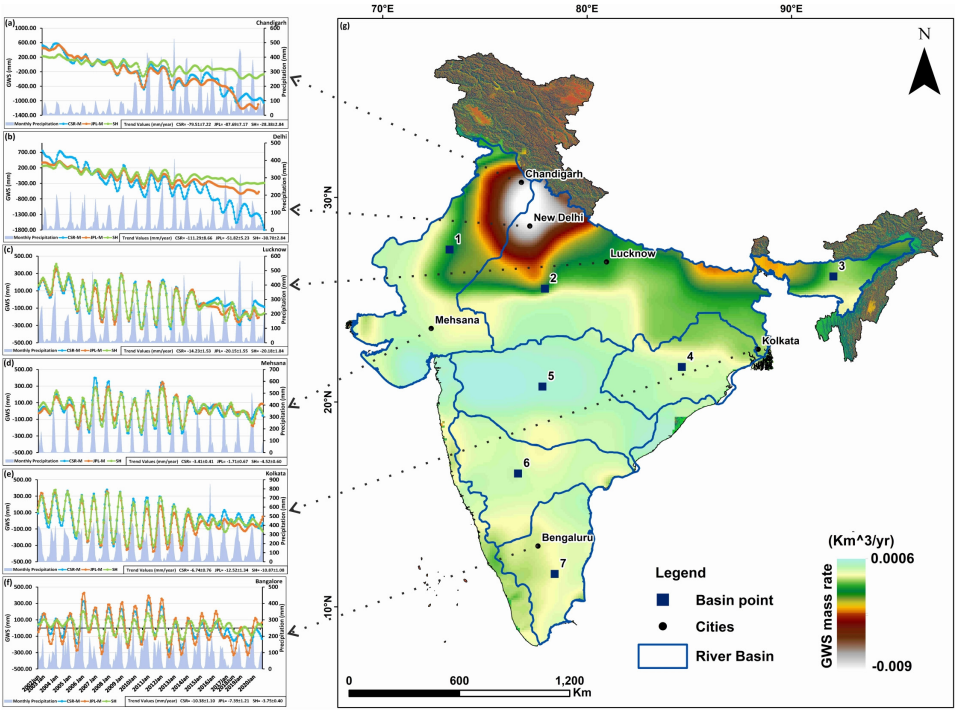

Fig. 7. The Indian cities; Chandigarh (a), Delhi (b), Mehsana (c), Kolkata (d), Lucknow (e) and Bengaluru (f) showing respective GWS change and amount of precipitation received by these regions (g) quantifying the deseasonalised GWS mass rate observed in all the seven basins (Basin 1–7) also showing variation in corresponding Indian cities (mentioned above).

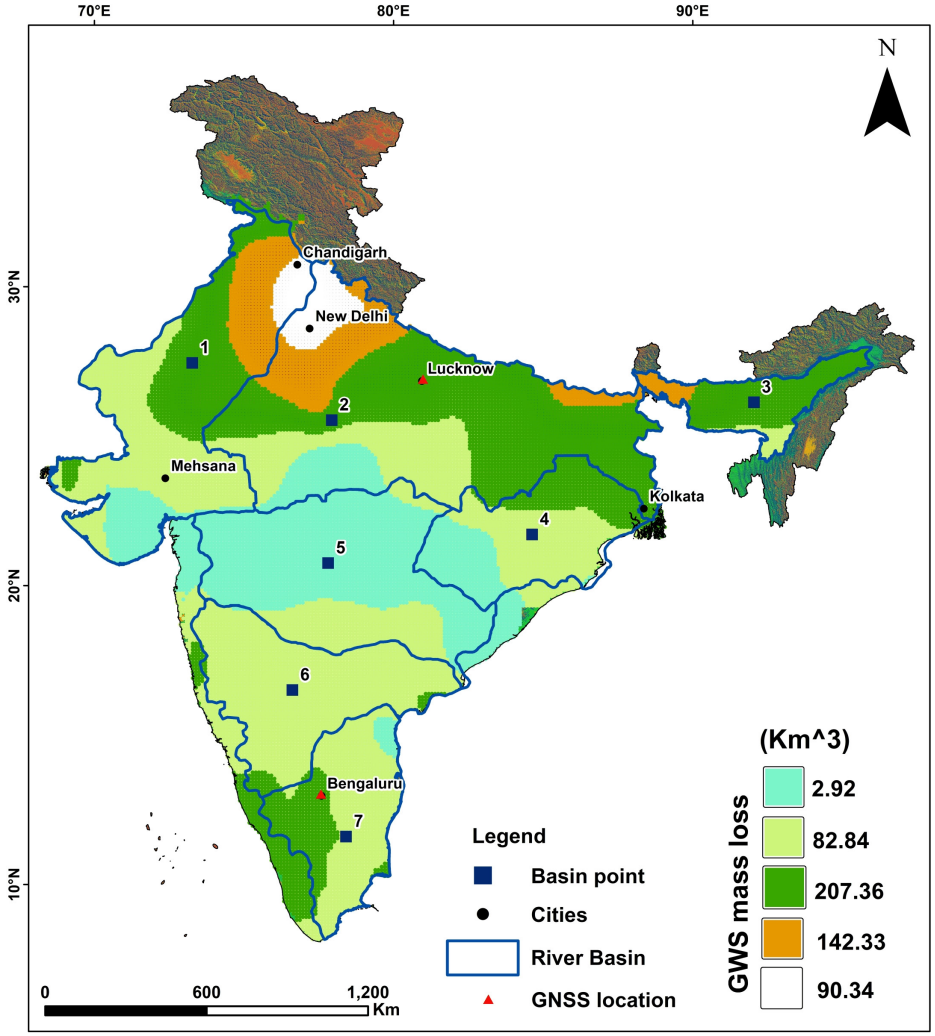

Fig. 8. The deseasonalized GWS mass loss (per grid) observed at seven basins (Basin 1–7) and six cities (Chandigarh, Delhi, Mehsana, Kolkata, Lucknow and Bengaluru). Note that the mass loss is high in and around the Basin 1 & 2 (New Delhi region) and lowest at Basin point 5.

(Fig. 7d). Kolkata, like Lucknow, shows a moderately low GWS mass rate and high rate of GWS depletion but experiences a comparatively poor

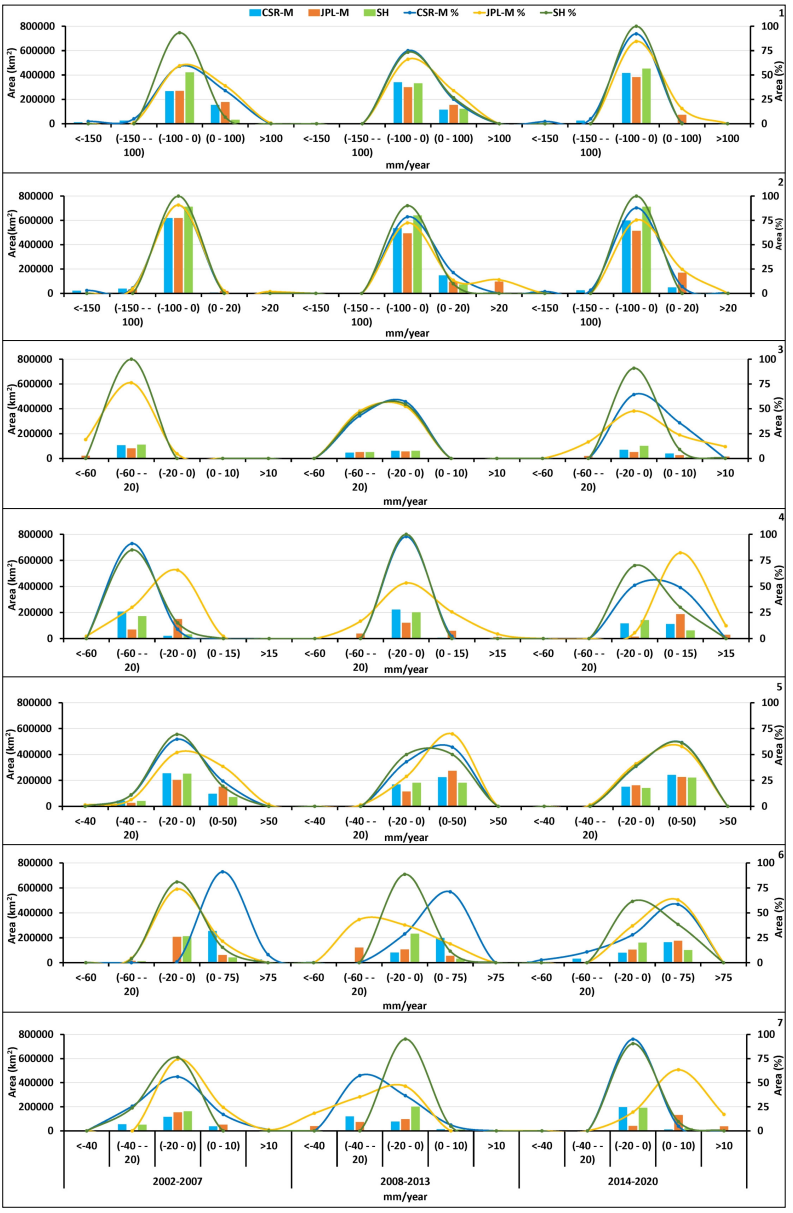

Fig. 9. The maximum percentage of the area (per grid) observing the rate of groundwater fluctuations in 2002–2007, 2008–2013, 2014-2020 periods in all seven basins (Basin 1–7).

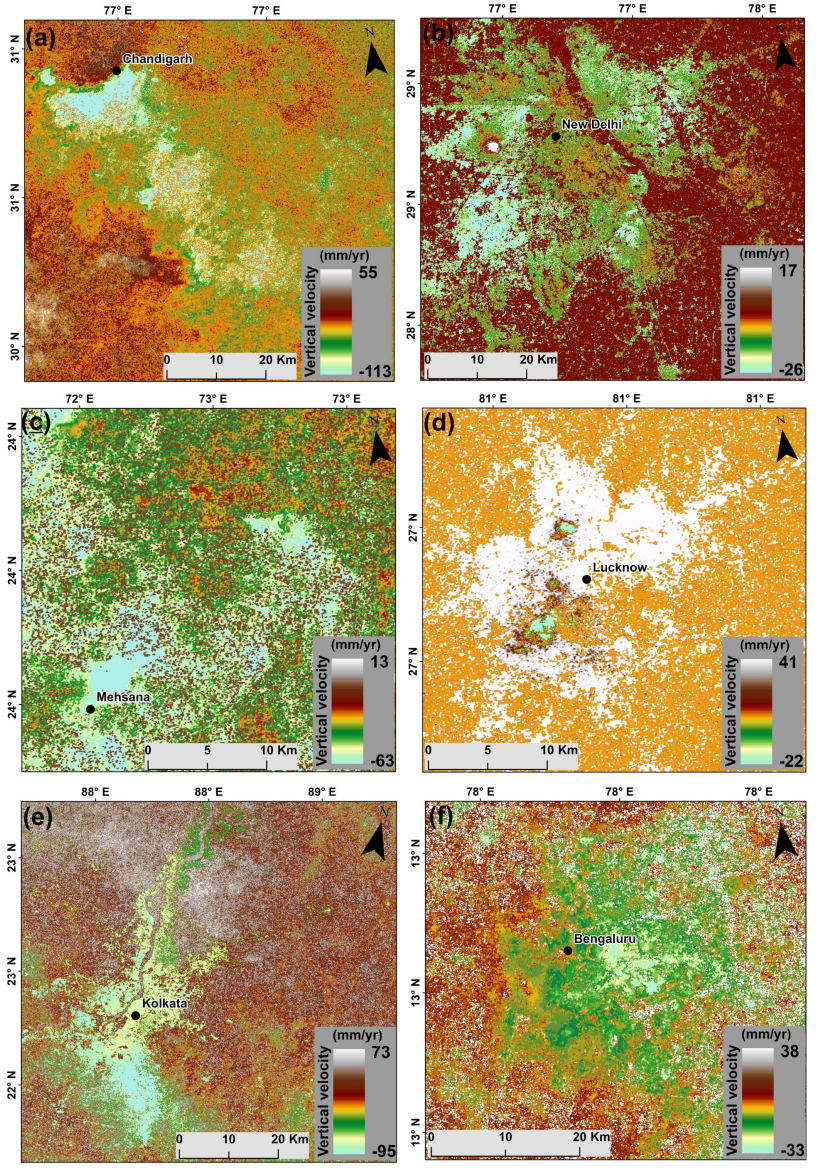

Fig. 10. The Ground deformation observed in Chandigarh (a), Delhi (b), Mehsana (c), Lucknow (d), Kolkata (e) and Bengaluru (f) due to GWS variation estimated using Sentinel-1A SAR data. The highest vertical velocity is estimated in Chandigarh (−113 mm/yr) and Kolkata (−95 mm/yr).

rainfall amount of ~ 300 mm (Fig. 7e). Finally, shifting towards South India, Bengaluru perceives a positive GWS mass rate (~ 0.0006 km^3/yr), very poor rainfall of ~ 100 mm with depleting GWS rate (Fig. 7f). As we know that mass loss represents the total volume of water leaving either by evapo-transpiration/runoff or being extracted from the aquifers to maintain increasing population and urbanization. In our study we have calculated deseasonalized GWS mass loss for over two decadal period (2002–2020). In this regard, from the 2D map (Fig. 8) it can be perceived that North Indian Cities are in utter groundwater crisis as they fall within that domain of river basin (1,2,3), experiencing the highest GWS mass loss especially in and around Chandigarh and New Delhi region, as compared to other Northern cities in respect to its areal extent. It has been observed that Bengaluru experiences significant mass loss despite being situated on Peninsular shield. Such anomalous situation can be explained either way 'i.e.,' GRACE data is unable to calculate groundwater variation at a local scale, so here the limitation arises with the spatial extent of this city. The other one could be the heterogeneous distribution of aquifers in this region. Subsequently observing a correlation between precipitation and GWS in seven basins, we found a positive correlation from 2002 to 2013. But from 2014–2020, all the basins exhibit a negative correlation between precipitation and GWS, which means rainfall is less (not that less for drought to occur) with decreasing GWS (Table 1).

The porosity of the sediments present underground is getting reduced as the confined layer lying above the aquifer is getting compacted. Such aquifer compaction or decline in the water table happens when groundwater gets extracted at very high rate which in return leads to land deformation. In this regard there are several leading instances globally (besides India) where over extraction of groundwater has led to severe land deformation especially in urban areas like Mexico, China, USA, Vietnam etc (*Holzer and Galloway, 2005; López-Quiroz et al., 2009; Chen et al., 2016; Bui et al., 2021*).

The effects of land deformation estimated from GPS (vertical displacement) and SAR derived vertical velocity is correlated with GWS mass change (Tables 2 & 3). The correlation results from SAR indicate that Delhi cannot balance the groundwater consumption (evident from GWS mass rate) and increasing population (*Gleeson et al., 2012; Sarkar et al., 2020*). The groundwater exploitation has started showing ground defor-

mation, which might be low initially, but down the line, it can escalate if groundwater use is not controlled.

6. Conclusion

India is a land of rivers that supports the residing population and livelihood. The demands for industries, advanced agricultural practices and urbanization are met by groundwater, thus becoming an essential resource for humankind. But this non-renewable resource is facing exploitation at such a rate that in specific years despite good rainfall, the groundwater rate depletes instead of rising. The drought intensity estimated using the Standardized Precipitation Index (a drought index indicator), which shows improved values from 2005-2020. But correspondingly in these years, GRACE & GRACE-FO (CSR-M, JPL-M, SH) derived GWS (per grid) observes fluctuation (maximum in Basins 1–4 than Basins 5–7). Next, we estimated the uncertainty of GWS both pixel/grid and basin wise at a 95% confidence level. The grid wise GWS estimation for 2002–2007, 2008–2013 and 2014–2020 show negative GWS trends, covering the maximum area of the rivers flowing in North. While the South Indian rivers affirm that positive GWS trends, covering the maximum of the grid area. All these significant changes started after 2014, and this paradox is explained by *Bhanja et al. (2017); Hora et al. (2019)*. Subsequently, we also monitored the long period groundwater fluctuation by decomposing the GWS time series using Seasonal Trend Decomposition (LOESS Regression) approach. In this process, we separated the Residuals comprising local phenomena (surface runoff, seeping of snow water etc.) which takes time to percolate and reach the water table through the vadose zone, also treated as noise/disturbances and the seasonal variation (monthly) to monitor the long-term groundwater storage change. The deseasonalized GWS mass rate (km^3/yr) observed in seven river basins is also studied over six respective Indian cities (Chandigarh, Delhi, Mehsana, Lucknow, Kolkata and Bengaluru) with respect to GWS change and precipitation received over there. In all the Northern cities or Basin 1–3, the GWS mass rate is moderate to low (-0.009 to < 0.0006), while the Central to Southern regions or Basin 4–7 affirms relatively high to moderate mass rate values. The deseasonalized GWS estimation (2002–2020) states that Himalayan River basins 1,2,3 exhibit high GWS mass loss (-260 to

-35.12 km^3), with Basin 2 being the highest (-260 km^3). Whereas the Peninsular River basin 4,6,7 gives moderate mass loss value from -26.72 to -23.58 km^3. And in River basin 5, the GWS mass loss observed is the lowest, with a value of -8 km^3.

We correlated GWS change with GPS data acquired from IISC & LCK3 IGS stations, and GWS mass rate (km^3/yr) with SAR (Sentinel 1A, SBAS) derived vertical velocity procured from Chandigarh, Delhi, Mehsana, Lucknow, Kolkata and Bengaluru to understand the effects of land deformation due to GWS mass loss. The correlation between GPS data and GWS mass is negative, resulting in $\sim -0.9 - (-) 0.21$ at IISC and $\sim -0.7 - (-) 0.41$ at LCK3 station (Table 3). Similarly, SAR correlates with the GWS mass rate showing the highest vertical velocity of -94.35 mm/yr in Kolkata, calculated from the positively correlated area. Although the highest vertical velocity is seen at the Kolkata region, Delhi (having comparatively very low vertical velocity, -25.73 mm/yr) still gives the highest GWS mass change, with Kolkata positioned at third rank after Lucknow (Table 4). There is an increase in population (estimated 2008–2014) in Basin 1 & 2. The correlation coefficient (r) between GWS change and the irrigational area is positive in all seven basins, implying an increase in GWS depletion due to an uncalled hike in population or irrigational land use. Similarly, the positive linear regression (R^2) in Basins 1–3 also indicates high depletion in GWS. But basins 4–7 observes negative linear regression even after increasing population, which implies a control on the irrigational land use, unable to determine the GWS change at local scale (as GRACE data is aggregated on a larger scale) and heterogeneous aquifer distribution in this area. Therefore, groundwater needs a proper strategic plan and controlled human intervention to stop getting parched shortly.

Acknowledgements. Our special appreciation to IGS/UNAVCO for helping us in GPS data acquisition, European Space Agency (ESA), for providing a platform to acquire Sentinel-1A data. We also acknowledge Mr. Bob King of MIT for GAMIT/GLOBK software that eases out GPS data processing, Climate hazards Centre, UC Santa Barbara for downloading CHIRPS data and Scripps Institute of Oceanography, San Diego for equipping us with the GMTSAR software. We also acknowledge those who have helped us in data acquisition, instrument installation and data processing directly or indirectly. The authors are also thankful to the critics who helped us accomplish this work. We would also like to acknowledge Editor-in-Chief Dr. Peter Vajda and anonymous reviewer for recognizing & appreciating our research work and providing us with critical sugges-

tions to resolve each and every mistakes. The authors would like to dedicate this work to Late Dr. P. K. Champati ray, whom we lost during the COVID-19 second wave. His vision and encouragement urged us to think innovatively and execute them as a contribution to society.

References

Aggarwal P. K., Joshi P. K., Ingram J. S. I., Gupta R. K., 2004: Adapting food systems of the Indo Gangetic plains to global environmental change Key information needs to improve policy formulation. Environ. Sci. Policy, **7**, 6, 487–498, doi: 10.1016/j.envsci.2004.07.006.

Andrew R., Guan H., Batelaan O., 2017: Estimation of GRACE water storage components by temporal decomposition. J. Hydrol., **552**, 341–350, doi: 10.1016/j.jhydrol.2017.06.016.

Asadi Zarch M. A., Sivakumar B., Sharma A., 2015: Droughts in a warming climate: A global assessment of Standardized precipitation index (SPI) and Reconnaissance drought index (RDI). J. Hydrol., **526**, 183–195, doi: 10.1016/j.jhydrol.2014.09.071.

Berardino P., Fornaro G., Lanari R., Sansosti E., 2002: A new algorithm for surface deformation monitoring based on small baseline differential SAR interferograms. IEEE Trans. Geosci. Remote Sens., **40**, 11, 2375–2383, doi: 10.1109/TGRS.2002.803792.

Bhanja S. N., Mukherjee A., Rodell M., Wada Y., Chattopadhyay S., Velicogna I., Pangaluru K., Famiglietti J. S., 2017: Groundwater rejuvenation in parts of India influenced by water-policy change implementation. Sci. Rep., **7**, 1, 7453, doi: 10.1038/s41598-017-07058-2.

Bhuiyan C., Singh R. P., Kogan F. N., 2006: Monitoring drought dynamics in the Aravalli region (India) using different indices based on ground and remote sensing data. Int. J. Appl. Earth Obs. Geoinf., **8**, 4, 289–302, doi: 10.1016/j.jag.2006.03.002.

Boergens E., Güntner A., Dobslaw H., Dahle C., 2020: Quantifying the Central European Droughts in 2018 and 2019 With GRACE Follow-On. Geophys. Res. Lett., **47**, 14, doi: 10.1029/2020GL087285.

Bui L. K., Le P. V. V., Dao P. D., Long N. Q., Pham H. V., Tran H. H., Xie L., 2021: Recent land deformation detected by Sentinel-1A InSAR data (2016–2020) over Hanoi, Vietnam, and the relationship with groundwater level change. GISci. Remote Sens., **58**, 2, 161–179, doi: 10.1080/15481603.2020.1868198.

Castellazzi P., Martel R., Rivera A., Huang J., Pavlic G., Calderhead A. I., Chaussard E., Garfias J., Salas J., 2016: Groundwater depletion in Central Mexico: Use of GRACE and InSAR to support water resources management. Water Resour. Res., **52**, 8, 5985–6003., doi: 10.1002/2015WR018211.

Central Ground Water Board (CGBW), 2012: Aquifer Systems of India (Government). New Delhi, http://cgwb.gov.in/AQM/.

Chaussard E., Wdowinski S., Cabral-Cano E., Amelung F., 2014: Land subsidence in central Mexico detected by ALOS InSAR time-series. Remote Sens. Environ., **140**, 94–106, doi: 10.1016/j.rse.2013.08.038.

Chen M., Tomás R., Li Z., Motagh M., Li T., Hu L., Gong H., Li X., Yu J., Gong X., 2016: Imaging Land Subsidence Induced by Groundwater Extraction in Beijing (China) Using Satellite Radar Interferometry. Remote Sens., 8, 6, 468, doi: 10.3390/rs8060468.

Chen Y., Tao Q., Hou A., Ding L., Liu G., Wang K., 2020: Accuracy verification and evaluation of Sentinel-1A repeat track differential interferometric synthetic aperture radar in monitoring mining subsidence. J. Appl. Remote Sens., 14, 1, 014501, doi: 10.1117/1.JRS.14.014501.

Cheo A. E., Voit H. J., Mbua R. L., 2013 **2012**: Climate change and the vulnerability of water resources in northern Cameroon. Tropentag 2012, September 19-21, 2012 in Göttingen, "Resilience of agricultural systems against crises", available at: https://www.tropentag.de/2012/abstracts/full/141.pdf.

Chinnasamy P., Hubbart J. A., Agoramoorthy G., 2013: Using Remote Sensing Data to Improve Groundwater Supply Estimations in Gujarat, India. Earth Interact., **17**, 1, 1–17, doi: 10.1175/2012EI000456.1.

Choudhury P., Gahalaut K., Dumka R., Gahalaut V. K., Singh A. K., Kumar S., 2018: GPS measurement of land subsidence in Gandhinagar, Gujarat (Western India), due to groundwater depletion. Environ. Earth Sci., **77**, 22, 770, doi: 10.1007/s12665-018-7966-5.

Cleveland R. B., Cleveland W. S., McRae J. E., Terpenning I., 1990: STL: A Seasonal-Trend Decomposition. J. Off. Stat., **6**, 1, 3–73. Retrieved from http://www.nniiem.ru/file/news/2016/stl-statistical-model.pdf.

Dhakar R., Sehgal V. K., Pradhan S., 2013: Study on inter-seasonal and intra-seasonal relationships of meteorological and agricultural drought indices in the Rajasthan State of India. J. Arid Environ., **97**, 108–119, doi: 10.1016/j.jaridenv.2013.06.001.

Ditmar P., 2018: Conversion of time-varying Stokes coefficients into mass anomalies at the Earth's surface considering the Earth's oblateness. J. Geod., **92**, 12, 1401–1412, doi: 10.1007/s00190-018-1128-0.

Döll P., Müller Schmied H., Schuh C., Portmann F. T., Eicker A., 2014: Global-scale assessment of groundwater depletion and related groundwater abstractions: Combining hydrological modeling with information from well observations and GRACE satellites. Water Resour. Res., **50**, 7, 5698–5720, doi: 10.1002/2014WR015595.

Foster S., Loucks D. P. (Eds.), 2006: Non-renewable groundwater resources: A guidebook on socially-sustainable management for water-policy makers. IHP-VI Ser. Groundwater10, U. N. Educ., Sci. and Cultural Organ., Paris, 103 p.

Funk C., Peterson P., Landsfeld M., Pedreros D., Verdin J., Shukla S., Husak G., Rowland J., Harrison L., Hoell A., Michaelsen J., 2015: The climate hazards infrared precipitation with stations—a new environmental record for monitoring extremes. Sci. Data, **2**, 150066, doi: 10.1038/sdata.2015.66.

Garg S., Motagh M., Jayaluxmi I., 2020: Land Subsidence in Delhi, India investigated using Sentinel-1 InSAR measurements. EGU General Assembly 2020, Online, 4–8 May 2020, EGU2020-21138, doi: 10.5194/egusphere-egu2020-21138.

Gautam P. K., Arora S., Kannaujiya S., Singh A., Goswami A., Champati P. K., 2017: A comparative appraisal of ground water resources using GRACE-GPS data in highly

urbanized regions of Uttar Pradesh, India. Sustain. Water Resour. Manag., **3**, 441–449, doi: 10.1007/s40899-017-0109-4.

Gleeson T., Wada Y., Bierkens M. F. P., van Beek L. P. H., 2012: Water balance of global aquifers revealed by groundwater footprint. Nature, **488**, 7410, 197–200, doi: 10.1038/nature11295.

Hafen R., 2016: Package 'stlplus': Enhanced Seasonal Decomposition of Time Series by Loess. Retrieved from: https://CRAN.R-project.org/package=stlplus, R package version 0.5.1.

Haque S., Kannaujiya S., Taloor A. K., Keshri D., Bhunia R. K., Champati Ray P. K., Chauhan P., 2020: Identification of groundwater resource zone in the active tectonic region of Himalaya through earth observatory techniques. Groundw. Sustain. Dev., Groundwater for Sustainable Development, **10**, 100337, doi: 10.1016/j.gsd.2020.100337.

Hoffmann J., Galloway D. L., Zebker H. A., 2003: Inverse modeling of interbed storage parameters using land subsidence observations, Antelope Valley, California. Water Resour. Res., **39**, 2, doi: 10.1029/2001WR001252.

Holzer T. L., Galloway D. L., 2005: Impacts of land subsidence caused by withdrawal of underground fluids in the United States (chapter 8). In: Ehlen J., Haneberg W. C., Larson R. A. (Eds.): Humans as Geologic Agents, Reviews in Engineering Geology, 16, 87–99, doi: https://doi.org/10.1130/2005.4016(08).

Hora T., Srinivasan V., Basu N. B., 2019: The Groundwater Recovery Paradox in South India. Geophys. Res. Lett., **46**, 16, 9602–9611, doi: 10.1029/2019gl083525.

Huang B., Shu L. Yang Y. S., 2012: Groundwater Overexploitation Causing Land Subsidence: Hazard Risk Assessment Using Field Observation and Spatial Modelling. Water Resour. Manag., **26**, 4225–4239, doi: 10.1007/s11269-012-0141-y.

Huizing H. G. J., 1971: A reconnaissance study of the mineralogy of sand fractions from East Pakistan sediments and soils. Geoderma, **6**, 2, 109–133, doi: 10.1016/0016-7061(71)90029-2.

Ittycheria N., Vaka D. S., Rao Y. S., 2018: Time series analysis of surface deformation of bengaluru city using sentinel-1 images. ISPRS Ann. Photogramm. Remote Sens. Spatial Inf. Sci., IV–5, 473–477, doi: 10.5194/isprs-annals-IV-5-473-2018.

Jain V. K., Pandey R. P., Jain M. K., Byun H.-R., 2015: Comparison of drought indices for appraisal of drought characteristics in the Ken River Basin. Weather Clim. Extremes, **8**, C, 1–11, doi: 10.1016/j.wace.2015.05.002.

Jasrotia A. S., Taloor A. K., Andotra U., Kumar R., 2019: Monitoring and assessment of groundwater quality and its suitability for domestic and agricultural use in the Cenozoic rocks of Jammu Himalaya, India: A geospatial technology based approach. Groundw. Sustain. Dev., **8**, 554–566, doi: 10.1016/j.gsd.2019.02.003.

Jekeli C., 1981: Modifying Stokes' function to reduce the error of geoid undulation computations. J. Geophys. Res. Solid Earth, **86**, B8, 6985–6990, doi: 10.1029/JB086iB08p06985.

Kannaujiya S., Gautam P. K., Champati ray P. K., Chauhan P., Roy P. N. S., Pal S. K., Taloor A. K., 2021: Contribution of seasonal hydrological loading in the variation

of seismicity and geodetic deformation in Garhwal region of Northwest Himalaya. Quat. Int., **575–576**, 62–71, doi: 10.1016/j.quaint.2020.04.049.

Kannaujiya S., Yadav R. K., Champati ray P. K., Sarkar T., Sharma G., Chauhan P., Pal S. K., Roy P. N. S., Gautam P. K., Taloor A. K., Yadav A., 2022: Unraveling seismic hazard by estimating prolonged crustal strain buildup in Kumaun-Garhwal, Northwest Himalaya using GPS measurements. J. Asian Earth Sci., **223**, 104993, doi: 10.1016/j.jseaes.2021.104993.

Karunakalage A., Sarkar T., Kannaujiya S., Chauhan P., Pranjal P., Taloor A. K., Kumar S., 2021: The appraisal of groundwater storage dwindling effect, by applying high resolution downscaling GRACE data in and around Mehsana district, Gujarat, India. Groundw. Sustain. Dev., **13**, 100559, doi: 10.1016/j.gsd.2021.100559.

Khorasani M., Ehteshami M., Ghadimi H., Salari M., 2016: Simulation and analysis of temporal changes of groundwater depth using time series modeling. Model. Earth Syst. Environ., **2**, 2, 90, 1–10, doi: 10.1007/s40808-016-0164-0.

Kumar M., Kumari K., Ramanathan A. L., Saxena R., 2007: A comparative evaluation of groundwater suitability for irrigation and drinking purposes in two intensively cultivated districts of Punjab, India. Environ. Geol., **53**, 3, 553–574, doi: 10.1007/s00254-007-0672-3.

Lafare A. E. A., Peach D. W., Hughes A. G., 2016: Use of seasonal trend decomposition to understand groundwater behaviour in the Permo-Triassic Sandstone aquifer, Eden Valley, UK. Hydrogeol. J., **24**, 1, 141–158, doi: 10.1007/s10040-015-1309-3.

Landerer F. W., Swenson S. C., 2012: Accuracy of scaled GRACE terrestrial water storage estimates. Water Resour. Res., **48**, 4, W04531, doi: 10.1029/2011WR011453.

Long D., Pan Y., Zhou J., Chen Y., Hou X., Hong Y., Scanlone B. R., Longuevergne L., 2017: Global analysis of spatiotemporal variability in merged total water storage changes using multiple GRACE products and global hydrological models. Remote Sens. Environ., **192**, 198–216, doi: 10.1016/j.rse.2017.02.011.

López-Quiroz P., Doin M.-P., Tupin F., Briole P., Nicolas J.-M., 2009: Time series analysis of Mexico City subsidence constrained by radar interferometry. J. Appl. Geophys., **69**, 1, 1–15, doi: 10.1016/j.jappgeo.2009.02.006.

Machiwal D., Jha M. K., Mal B. C., 2011: Assessment of Groundwater Potential in a Semi-Arid Region of India Using Remote Sensing, GIS and MCDM Techniques. Water Resour. Manag., **25**, 5, 1359–1386, doi: 10.1007/s11269-010-9749-y.

Margat J., van der Gun J., 2013: Groundwater around the World: A Geographic Synopsis. Taylor and Francis, London, U.K, 376 p.

McGuire V. L., 2009: Water-level changes in the High Plains Aquifer, predevelopment to 2007, 2005–06, and 2006–2007. U.S. Geol. Surv. Sci. Invest. Rep., 2009–5019, 9 p., US Geological Survey, Washington, D.C.

McKee T. B., Doesken N. J., Kleist J., 1993: The relationship of drought frequency and duration to time scales. In: Proceedings of the 8th Conference on Applied Climatology, Anaheim, California, 17-22 January 1993, **17**, 22, 179–183.

Mishra A. K., Singh V. P., 2010: A review of drought concepts. J. Hydrol., **391**, 1-2, 202–216, doi: 10.1016/j.jhydrol.2010.07.012.

Misra A. K., Saxena A., Yaduvanshi M., Mishra A., Bhadauriya Y., Thakur A., 2007: Proposed river-linking project of India: a boon or bane to nature. Environ. Geol., **51**, 8, 1361–1376, doi: 10.1007/s00254-006-0434-7.

Mukherjee A., Saha D., Harvey C. F., Taylor R. G., Ahmed K. M., Bhanja S. N., 2015: Groundwater systems of the Indian Sub-Continent. J. Hydrol., Regional Studies, **4**, Part A, 1–14, doi: 10.1016/j.ejrh.2015.03.005.

Naqvi S. M., Sawkar R. H., Subba Rao D. V., Govil P. K., Gnaneswar Rao T., 1988: Geology, geochemistry and tectonic setting of Archaean greywackes from Karnataka nucleus, India. Precambrian Res., **39**, 3, 193–216, doi: 10.1016/0301-9268(88)90042-3.

National Rainfed Area Authority (NRAA), 2013: Contingency and Compensatory Agriculture Plans for Droughts and Floods in India 2012. Position paper No. 6. National Rainfed Area Authority, NASC Complex, DPS Marg, New Delhi, pp. 87.

Neves M. C., Nunes L. M., Monteiro J. P., 2020: Evaluation of GRACE data for water resource management in Iberia: a case study of groundwater storage monitoring in the Algarve region. J. Hydrol. Reg. Stud., **32**, 100734, doi: 10.1016/j.ejrh.2020.100734.

Ojha C., Werth S., Shirzaei M., 2019: Groundwater Loss and Aquifer System Compaction in San Joaquin Valley During 2012–2015 Drought. J. Geophys. Res. Solid Earth, **124**, 3, 3127–3143, doi: 10.1029/2018JB016083.

Panda D. K., Ambast S. K., Shamsudduha M., 2020: Groundwater depletion in northern India: Impacts of the sub-regional anthropogenic land-use, socio-politics and changing climate. Hydrol. Process., **35**, 2, e14003, doi: 10.1002/hyp.14003.

Parthasarathy B., Sontakke N. A., Monot A. A., Kothawale D. R., 1987: Droughts/floods in the summer monsoon season over different meteorological subdivisions of India for the period 1871–1984. J. Climatol., **7**, 1, 57–70, doi: 10.1002/joc.3370070106.

Peiris T. S. G., Seneviratne E. K., 2010: An Alternative Approach for Analysis of Data from a Long-Term Experiment. COCOS, **7**, 14–20, doi: 10.4038/cocos.v7i0.2058.

Priyan K., 2015: Spatial and Temporal Variability of Rainfall in Anand District of Gujarat State. Aquatic Procedia, **4**, 713–720, doi: 10.1016/j.aqpro.2015.02.092.

Reager J. T., Gardner A. S., Famiglietti J. S., Wiese D. N., Eicker A., Lo M.-H., 2016: A decade of sea level rise slowed by climate-driven hydrology. Science, **351**, 6274, 699–703, doi: 10.1126/science.aad8386.

Rodell M., Famiglietti J. S., 2002: The potential for satellite-based monitoring of groundwater storage changes using GRACE: the High Plains aquifer, Central US. J. Hydrol., **263**, 1-4, 245–256, doi: 10.1016/S0022-1694(02)00060-4.

Rodell M., Velicogna I., Famiglietti J. S., 2009: Satellite-based estimates of groundwater depletion in India. Nature, **460**, 999–1002, doi: 10.1038/nature08238.

Rodell M., Chen J., Kato H., Famiglietti J. S., Nigro J., Wilson C. R., 2007: Estimating groundwater storage changes in the Mississippi River basin (USA) using GRACE. Hydrogeol. J., **15**, 1, 159–166, doi: 10.1007/s10040-006-0103-7.

Rosen P. A., Hensley S., Joughin I. R., Li F. K., Madsen S. N., Rodriguez E., Goldstein R. M., 2000: Synthetic aperture radar interferometry. Proc. IEEE, **88**, 3, 333–382, doi: 10.1109/5.838084.

Rowlands D. D., Luthcke S. B., McCarthy J. J., Klosko S. M., Chinn D. S., Lemoine F. G., Boy J.-P., Sabaka T. J., 2010: Global mass flux solutions from GRACE: A comparison of parameter estimation strategies—Mass concentrations versus stokes coefficients, J. Geophys. Res. Solid Earth, **115**, B1, B01403, doi: 10.1029/2009JB006546.

Sahu P., Sikdar P. K., 2011: Threat of land subsidence in and around Kolkata City and East Kolkata Wetlands, West Bengal, India. J. Earth Syst. Sci., **120**, 3, 435–446, doi: 10.1007/s12040-011-0077-2.

Samra J. S., 2004: Review and analysis of drought monitoring, declaration and management in India. Working Paper 84, International Water Management Institute, Colombo, Sri Lanka.

Sarkar T., Kannaujiya S., Taloor A. K., Champati Ray P. K., Chauhan P., 2020: Integrated study of GRACE data derived interannual groundwater storage variability over water stressed Indian regions. Groundw. Sustain. Dev., **10**, 100376, doi: 10.1016/j.gsd.2020.100376.

Save H., Bettadpur S., Tapley B. D., 2016: High-resolution CSR GRACE RL05 mascons. J. Geophys. Res. Solid Earth, **121**, 10, 7547–7569, doi: 10.1002/2016JB013007.

Scanlon B. R., Faunt C. C., Longuevergne L., Reedy R. C., Alley W. M., McGuire V. L., McMahon P. B., 2012: Groundwater depletion and sustainability of irrigation in the US High Plains and Central Valley. Proceedings of the National Academy of Sciences, **109**, 24, 9320–9325, doi: 10.1073/pnas.1200311109.

Scanlon B. R., Zhang Z., Save H., Wiese D. N., Landerer F. W., Long D., Longuevergne L., Chen J., 2016: Global evaluation of new GRACE mascon products for hydrologic applications. Water Resour. Res., **52**, 12, 9412–9429, doi: 10.1002/2016wr019494.

Seeyan S., Merkel B., Abo R., 2014: Investigation of the Relationship between Groundwater Level Fluctuation and Vegetation Cover by using NDVI for Shaqlawa Basin, Kurdistan Region – Iraq. J. Geogr. Geol., **6**, 3, doi: 10.5539/jgg.v6n3p187.

Sneed M., Ikehara M. E., Galloway D. L., Amelung F., 2001: Detection and measurement of land subsidence using global positioning system and interferometric synthetic aperture radar, Coachella Valley, California, 1996–98. U.S. Geological Survey, Water-Resources Investigations Report 2001–4193, 26 p., doi: 10.3133/wri014193.

Spinoni J., Vogt J. V., Naumann G., Barbosa P., Dosio A., 2018: Will drought events become more frequent and severe in Europe? Int. J. Climatol., **38**, 4, 1718–1736, doi: 10.1002/joc.5291.

Suganthi S., Elango L., 2020: Estimation of groundwater abstraction induced land subsidence by SBAS technique. J. Earth Syst. Sci., **129**, 1, 46, 1–13, doi: 10.1007/s12040-019-1298-z.

Swenson S., Wahr J., 2006: Post-processing removal of correlated errors in GRACE data. Geophys. Res. Lett., **33**, 8, L08402, doi: 10.1029/2005GL025285.

Tapley B. D., Bettadpur S., Ries J. C., Thompson P. F., Watkins M. M., 2004: GRACE Measurements of Mass Variability in the Earth System. Science, **305**, 5683, 503–505, doi: 10.1126/science.1099192.

Thomas A. C., Reager J. T., Famiglietti J. S., Rodell M., 2014: A GRACE-based water storage deficit approach for hydrological drought characterization. Geophys. Res. Lett., **41**, 5, 1537–1545, doi: 10.1002/2014GL059323.

Torres R., Snoeij P., Geudtner D., Bibby D., Davidson M., Attema E., Potin P., Rommen B., Floury N., Brown M., Traver I. N., Deghaye P., Duesmann B., Rosich B., Miranda N., Bruno C., L'Abbate M., Croci R., Pietropaolo A., Huchler M., Rostan F., 2012: GMES Sentinel-1 mission. Remote Sens. Environ., **120**, 9–24, doi: 10.1016/j.rse.2011.05.028.

Van Loon A. F., 2015: Hydrological drought explained. WIREs Water, **2**, 4, 359–392, doi: 10.1002/wat2.1085.

Vasco D. W., Farr T. G., Jeanne P., Doughty C., Nico P., 2019: Satellite-based monitoring of groundwater depletion in California's Central Valley. Sci. Rep., **9**, 16053, doi: 10.1038/s41598-019-52371-7.

Velicogna I., Mohajeran Y., Geruo A., Landerer F., Mouginot J., Noel B., Rignot E., Sutterley T., van den Broeke M., van Wessem M., Wiese D., 2020: Continuity of Ice Sheet Mass Loss in Greenland and Antarctica From the GRACE and GRACE Follow-On Missions. Geophys. Res. Lett., **47**, 8, e2020GL087291, doi: 10.1029/2020GL087291.

Wahr J., Molenaar M., Bryan F., 1998: Time variability of the Earth's gravity field: Hydrological and oceanic effects and their possible detection using GRACE. J. Geophys. Res. Solid Earth, **103**, B12, 30205–30229, doi: 10.1029/98JB02844.

Wahr J., Swenson S., Velicogna I., 2006: Accuracy of GRACE mass estimates. Geophys. Res. Lett., **33**, 6, L06401, doi: 10.1029/2005GL025305.

Wang L., Chen C., Du J., Wang T., 2017: Detecting seasonal and long-term vertical displacement in the North China Plain using GRACE and GPS. Hydrol. Earth Syst. Sci., **21**, 6, 2905–2922, doi: 10.5194/hess-21-2905-2017.

Watkins M. M., Wiese D. N., Yuan D.-N., Boening C., Landerer F. W., 2015: Improved methods for observing Earth's time variable mass distribution with GRACE using spherical cap mascons. J. Geophys. Res. Solid Earth, **120**, 4, 2648–2671, doi: 10.1002/2014JB011547.

Whiteman M., Brooks A., Skinner A., Hulme P., 2010: Determining significant damage to groundwater-dependent terrestrial ecosystems in England and Wales for use in implementation of the Water Framework Directive. Ecol. Eng., **36**, 9, 1118–1125, doi: 10.1016/j.ecoleng.2010.03.013.

Wiese D. N., Landerer F. W., Watkins M. M., 2016: Quantifying and reducing leakage errors in the JPL RL05M GRACE mascon solution. Water Resour. Res., **52**, 9, 7490–7502, doi: 10.1002/2016WR019344.

Wilhite D. A., Glantz M. H., 1985: Understanding: the Drought Phenomenon: The Role of Definitions. Water Int., **10**, 3, 111–120, doi: 10.1080/02508068508686328.

Yadav A., Kannaujiya S., Champati ray P. K., Yadav R. K., Gautam P. K., 2021: Estimation of crustal deformation parameters and strain build-up in Northwest Himalaya using GNSS data measurements. Contrib. Geophys. Geod., **51**, 3, 225–243, doi: 10.31577/congeo.2021.51.3.2.

Appendix

Supplementary tables

Table S1. Data parameters used for estimation of drought, GWS, and vertical deformation in the seven river basins (Basin 1-7).

Hydroclimatic Data					
Data Type	Data Source	Data Model	Period	Resolution	
				Spatial	Temporal
GRACE Mascon	NASA Earth Data (GRACE Mission, GRACE-FO Mission)	CSR JPL	2002–2020	25km ×25km 50km ×50km	Monthly
Tellus Gridded GRACE Spherical Harmonic	NASA Earth Data (GRACE Mission, GRACE-FO Mission)	Level 3 (RL06) CSR JPL SH	2002–2020	100km ×100km	Monthly
Total Water Content	Global Land Data Assimilation System (GLDAS)	NOAH 2.1	2002–2020	50km ×50km	Monthly
Rainfall	Climate Hazards Group InfraRed Precipitation with Station (CHIRPS)	v 2.0	2002–2020	5km ×5km	Monthly

Global Positioning System (GPS)		
Data Source	Station	Period
International GNSS Service (IGS)	Bengaluru	2017–2020
	Lucknow	

Interferometric SAR				
Satellite Name	Data Source	Total Processed Tiles	Target City	Period
Sentinel 1A (European Space Agency)	Alaskan Satellite Facility	39	Chandigarh	2016–2020 Pre-monsoon
			New Delhi	
			Mehsana	
			Lucknow	
			Kolkata	

Table S2. (a) to (g) features percentage of area related to different groundwater storage fluctuations which have been derived from GRACE mascon and SH solutions for three different periods in each basin (Basin 1–7) for periods; 2002–2007, 2008–2013, 2014–2020.

S2 (a) for basin 1

Groundwater Storage rate (mm/yr)	Period																	
	2002–2007						2008–2013						2014–2020					
	Mascon				SH		Mascon				SH		Mascon				SH	
	CSR		JPL				CSR		JPL				CSR		JPL			
	Area	%	Area	%	Area	%	Area	%	Area	%	Area	%	Area	%	Area	%	Area	%
<-150	10000	2	0	0	0	0	0	0	0	0	0	0	10000	2	0	0	0	0
(-150 – -100)	22500	5	5000	1	0	0	0	0	0	0	0	0	22500	5	0	0	0	0
(-100 – -50)	32500	7	65000	14	20000	4	35000	8	15000	3	0	0	75000	17	35000	8	0	0
(-50-0)	232500	52	202500	45	400000	89	302500	67	282500	63	330000	73	340000	76	345000	77	450000	100
(0–100)	152500	34	175000	39	30000	7	112500	5	152500	34	120000	27	2500	1	70000	16	0	0
>100	0	0	2500	1	0	0	0	0	0	0	0	0	0	0	0	0	0	0

S2 (b) for basin 2

Groundwater Storage rate (mm/yr)	Period																	
	2002–2007						2008–2013						2014–2020					
	Mascon				SH		Mascon				SH		Mascon				SH	
	CSR		JPL		Area	%	CSR		JPL		Area	%	CSR		JPL		Area	%
	Area	%	Area	%			Area	%	Area	%			Area	%	Area	%		
<-150	20000	3	0	0	0	0	0	0	0	0	0	0	12500	2	0	0	0	0
(-150 – 100)	37500	6	32500	5	0	0	0	0	0	0	0	0	22500	3	0	0	0	0
(-100 – -50)	130000	19	252500	37	90000	13	45000	7	37500	6	0	0	35000	5	37500	6	0	0
(-50 – 0)	487500	72	365000	54	620000	87	490000	72	455000	67	640000	90	562500	83	475000	70	710000	100
(0 – 20)	5000	1	17500	3	0	0	145000	21	92500	14	70000	10	47500	7	167500	25	0	0
>20	0	0	12500	2	0	0	0	0	95000	14	0	0	0	0	0	0	0	0

S2 (c) for basin 3

Groundwater Storage rate (mm/yr)	Period																	
	2002–2007						2008–2013						2014–2020					
	Mascon				SH		Mascon				SH		Mascon				SH	
	CSR		JPL		Area	%	CSR		JPL		Area	%	CSR		JPL		Area	%
	Area	%	Area	%			Area	%	Area	%			Area	%	Area	%		
<-60	0	0	20000	19	0	0	0	0	0	0	0	0	0	0	0	0	0	0
(-60 – -40)	22500	21	27500	26	40000	36	10000	10	35000	33	0	0	0	0	0	0	0	0
(-40 – -20)	82500	79	52500	50	70000	64	35000	33	15000	14	50000	45	0	0	17500	17	0	0
(-20 – 0)	0	0	5000	5	0	0	60000	57	55000	52	60000	55	67500	64	50000	48	100000	91
(0 – 10)	0	0	0	0	0	0	0	0	0	0	0	0	37500	36	25000	24	10000	9
>10	0	0	0	0	0	0	0	0	0	0	0	0	0	0	12500	12	0	0

S2 (d) for basin 4

Groundwater Storage rate (mm/yr)	Period																	
	2002–2007						2008–2013						2014–2020					
	Mascon				SH		Mascon				SH		Mascon				SH	
	CSR		JPL		Area	%	CSR		JPL		Area	%	CSR		JPL		Area	%
	Area	%	Area	%			Area	%	Area	%			Area	%	Area	%		
<-60	0	0	5000	2	0	0	0	0	0	0	0	0	0	0	0	0	0	0
(-60 – -40)	0	0	62500	28	0	0	0	0	0	0	0	0	0	0	0	0	0	0
(-40 – -20)	205000	91	5000	2	170000	85	0	0	37500	17	0	0	0	0	0	0	0	0
(-20 – 0)	20000	9	147500	66	30000	15	220000	98	120000	53	200000	100	115000	51	12500	6	140000	70
(0 – 15)	0	0	5000	2	0	0	5000	2	57500	26	0	0	110000	49	185000	82	60000	30
>15	0	0	0	0	0	0	0	0	10000	4	0	0	0	0	27500	12	0	0

S2 (e) for basin 5

Groundwater Storage rate (mm/yr)	Period																	
	2002–2007						2008–2013						2014–2020					
	Mascon				SH		Mascon				SH		Mascon				SH	
	CSR		JPL		Area	%	CSR		JPL		Area	%	CSR		JPL		Area	%
	Area	%	Area	%			Area	%	Area	%			Area	%	Area	%		
<-60	0	0	5000	2	0	0	0	0	0	0	0	0	0	0	0	0	0	0
(-60 – -40)	0	0	62500	28	0	0	0	0	0	0	0	0	0	0	0	0	0	0
(-40 – -20)	205000	91	5000	2	170000	85	0	0	37500	17	0	0	0	0	0	0	0	0
(-20 – 0)	20000	9	147500	66	30000	15	220000	98	120000	53	200000	100	115000	51	12500	6	140000	70
(0 – 15)	0	0	5000	2	0	0	5000	2	57500	26	0	0	110000	49	185000	82	60000	30
>15	0	0	0	0	0	0	0	0	10000	4	0	0	0	0	27500	12	0	0

S2 (f) for basin 6

Groundwater Storage rate (mm/yr)	Period																	
	2002–2007						2008–2013						2014–2020					
	Mascon				SH		Mascon				SH		Mascon				SH	
	CSR		JPL				CSR		JPL				CSR		JPL			%
	Area	%	Area	%	Area	%	Area	%	Area	%	Area	%	Area	%	Area	%	Area	
<-60	0	0	0	0	0	0	0	0	0	0	0	0	7500	3	0	0	0	0
(-60 – -40)	0	0	0	0	0	0	0	0	2500	1	0	0	2500	1	0	0	0	0
(-40 – -20)	0	0	12500	5	10000	4	0	0	117500	42	0	0	27500	10	0	0	0	0
(-20 – 0)	2500	1	205000	74	210000	81	80000	29	105000	38	230000	88	77500	28	102500	37	160000	62
(0 – 75)	252500	91	60000	22	40000	15	197500	71	52500	19	30000	12	162500	59	175000	63	100000	38
>75	22500	8	0	0	0	0	0	0	0	0	0	0	0	0	0	0	0	0

S2 (g) for basin 7

Groundwater Storage rate (mm/yr)	Period																	
	2002–2007						2008–2013						2014–2020					
	Mascon				SH		Mascon				SH		Mascon				SH	
	CSR		JPL				CSR		JPL				CSR		JPL			
	Area	%	Area	%	Area	%	Area	%	Area	%	Area	%	Area	%	Area	%	Area	%
<-40	0	0	0	0	0	0	0	0	37500	18	0	0	0	0	0	0	0	0
(-40 – -20)	52500	26	0	0	50000	24	117500	57	72500	35	0	0	0	0	0	0	0	0
(-20 – 0)	115000	56	152500	74	160000	76	75000	37	95000	46	200000	95	195000	95	40000	20	190000	90
(0 – 5)	12500	6	25000	12	0	0	7500	4	0	0	10000	5	7500	4	105000	51	20000	10
(5 – 10)	22500	11	25000	12	0	0	5000	2	0	0	0	0	2500	1	25000	12	0	0
>10	2500	1	2500	1	0	0	0	0	0	0	0	0	0	0	35000	17	0	0

Supplementary figures

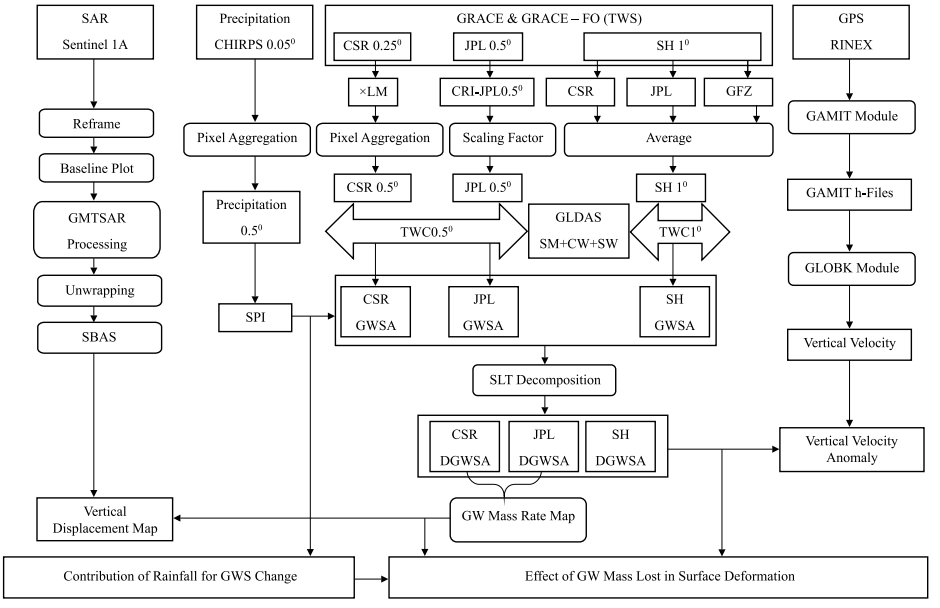

Fig. S1. Flowchart showing the different data and the respective methods used to estimate GWS, Drought Index, Vertical velocity and Vertical displacement in seven river basins (Basin 1–7).

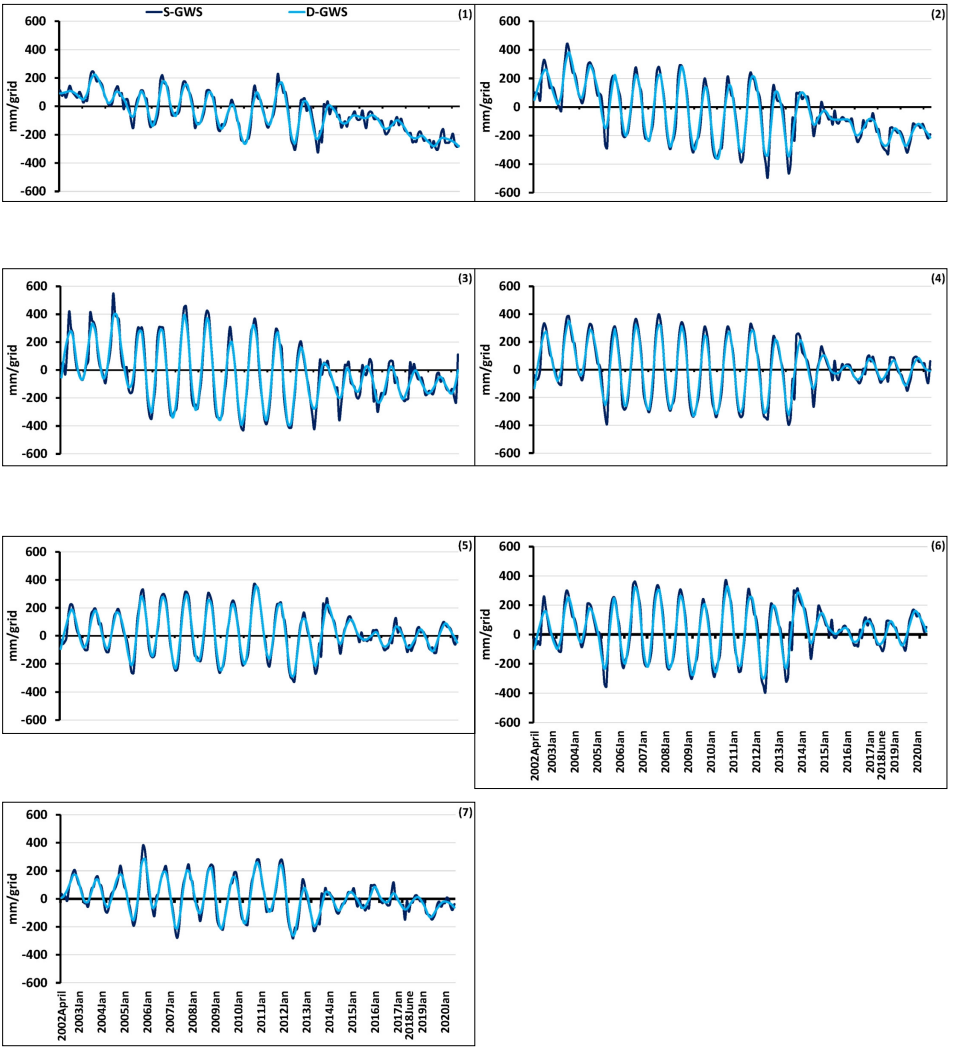

Fig. S2. (a) Deseasonalization shown by CSR-M using (STL) Seasonal Trend decomposition in all seven river basins (Basin 1–7).

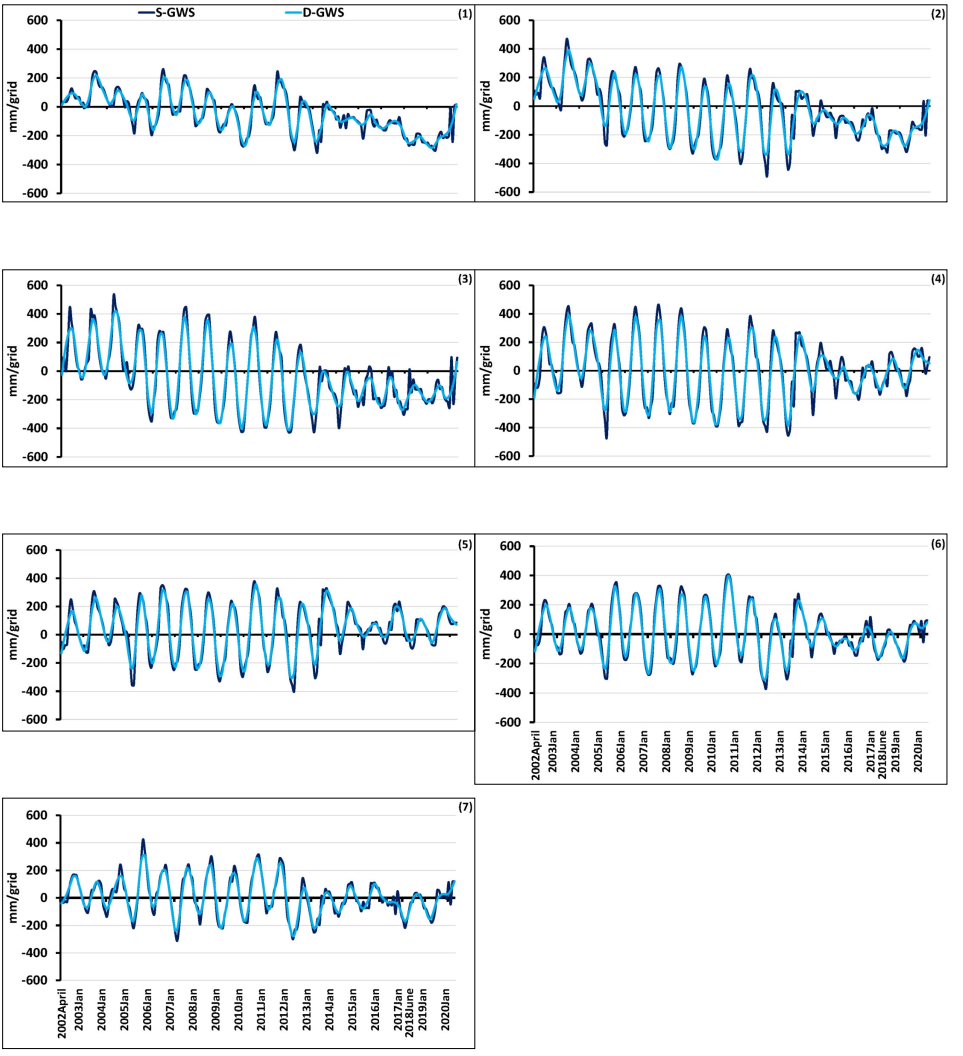

Fig. S2. (b) Deseasonalization shown by JPL-M using (STL) Seasonal Trend decomposition in all the seven river basins (Basin 1–7).

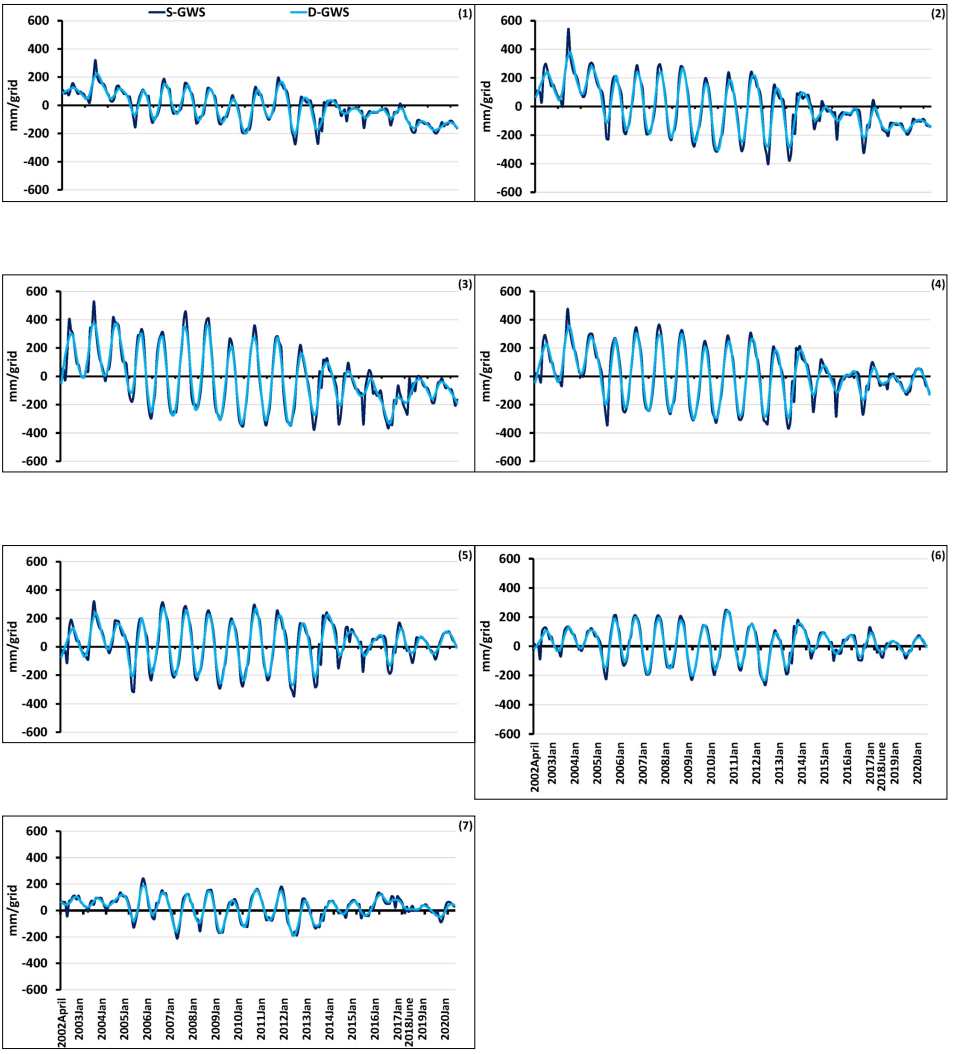

Fig. S2. (c) Deseasonalization shown by SH using (STL) Seasonal Trend decomposition in seven river basins (Basin 1–7).

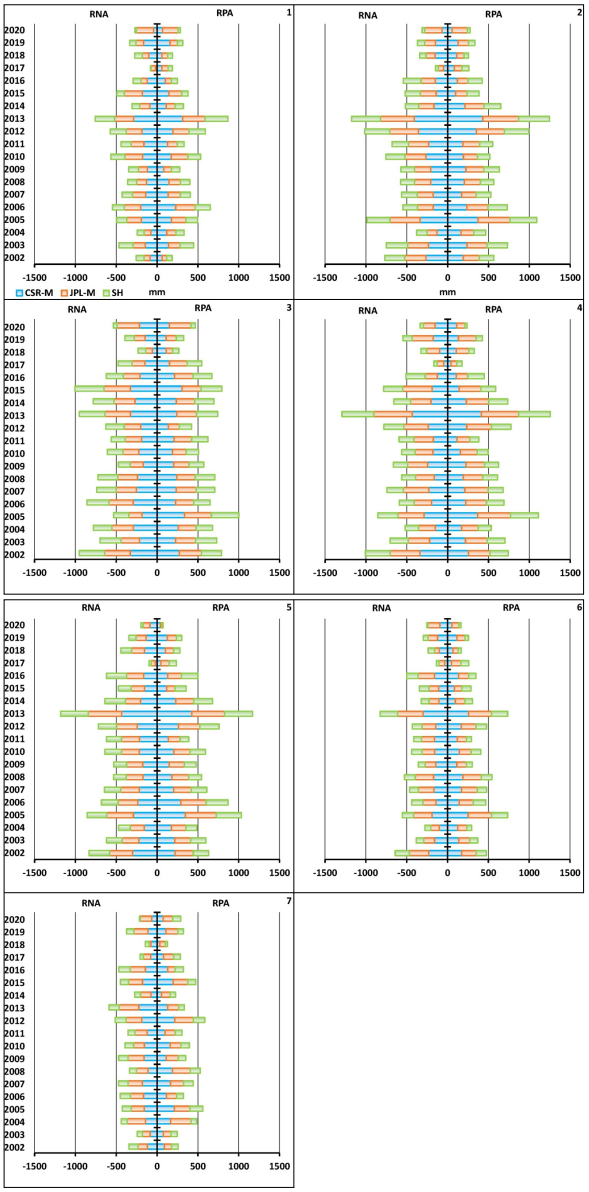

Fig. S3. Residuals estimated after applying STL decomposition on GWS time series (where seasonal component is embedded) showing Residual Positive Amplitude (RPA) and Residual Negative Amplitude (RNA) by CSR-M, JPL-M and SH in all the seven basins (Basin 1–7) individually.

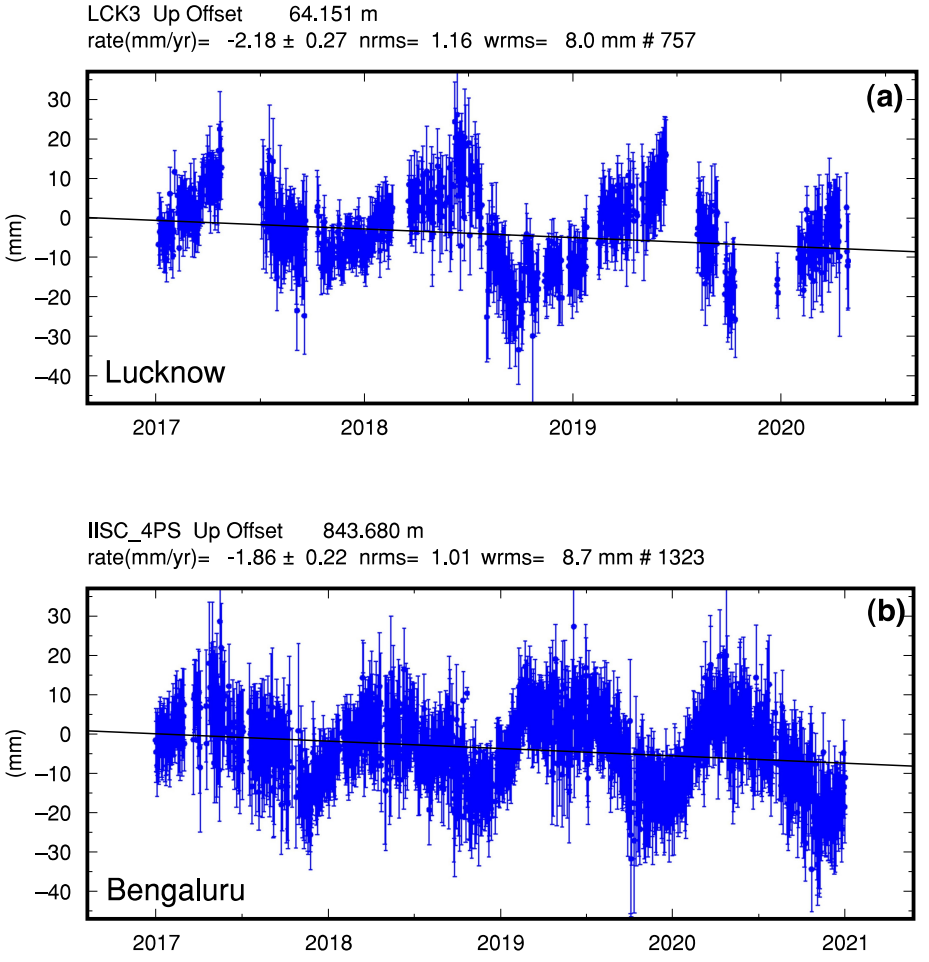

Fig. S4. The GPS displacement is estimated from IGS stations (a) LCK3 Lucknow (b) and IISC Bengaluru with respect to ITRF2014 to validate the results of land deformation obtained from SAR Sentinel 1A data analysis.

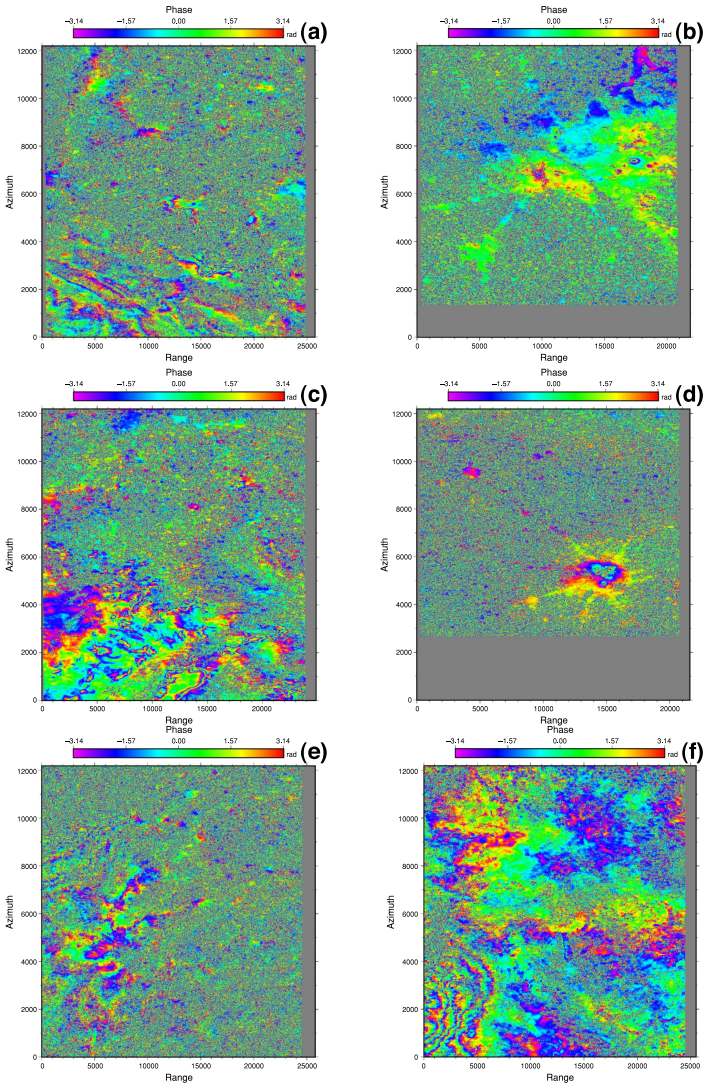

Fig. S5. (a) Interferograms developed during Sentinel 1A data processing showing phase change at Chandigarh. (b) Interferograms developed during Sentinel 1A data processing showing phase change at Delhi. (c) Interferograms developed during Sentinel 1A data processing showing phase change at Mehsana (d) Interferograms developed during Sentinel 1A data processing showing phase change at Lucknow. (e) Interferograms developed during Sentinel 1A data processing showing phase change at Kolkata. (f) Interferograms developed during Sentinel 1A data processing showing phase change at Bengaluru.

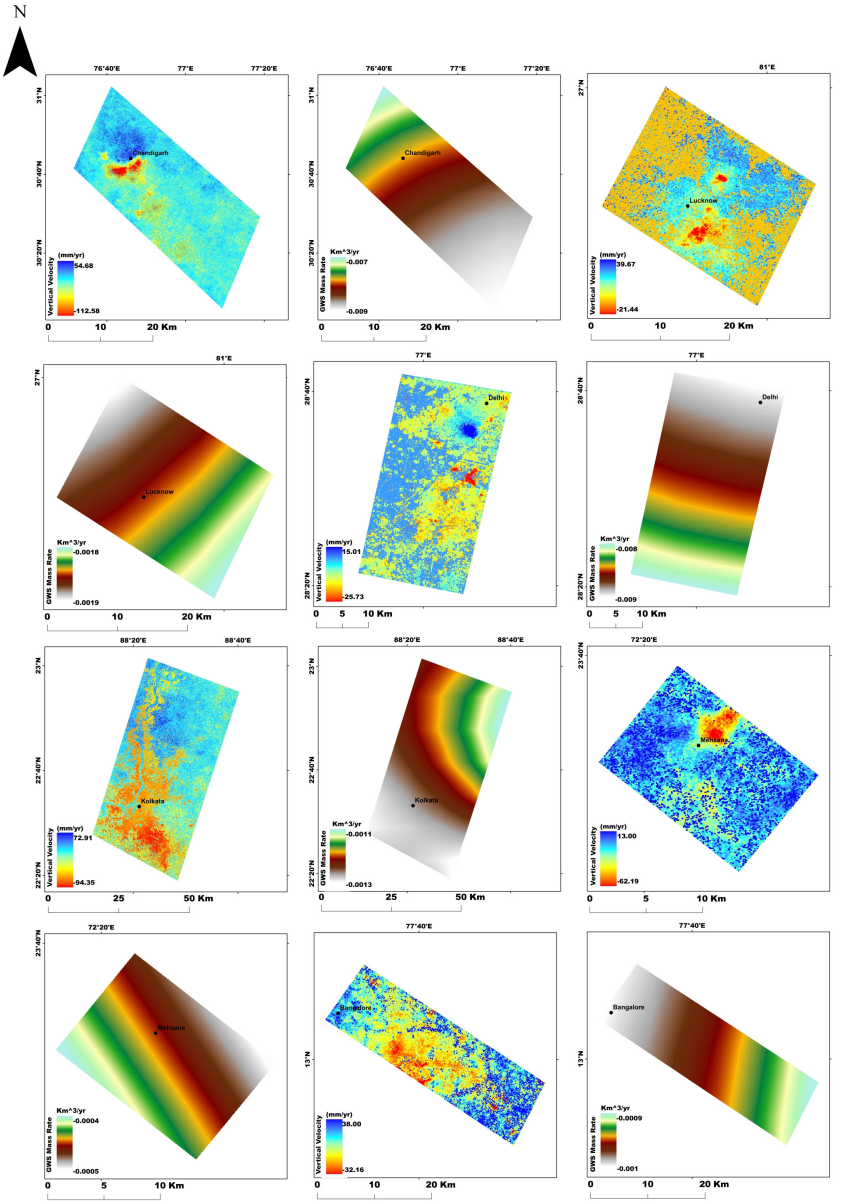

Fig. S6. Correlation between SAR derived vertical velocity and GWS mass rate in Chandigarh, Delhi, Mehsana, Lucknow, Kolkata, Bengaluru to analyse and assess the effect of land deformation due to overextraction of groundwater.

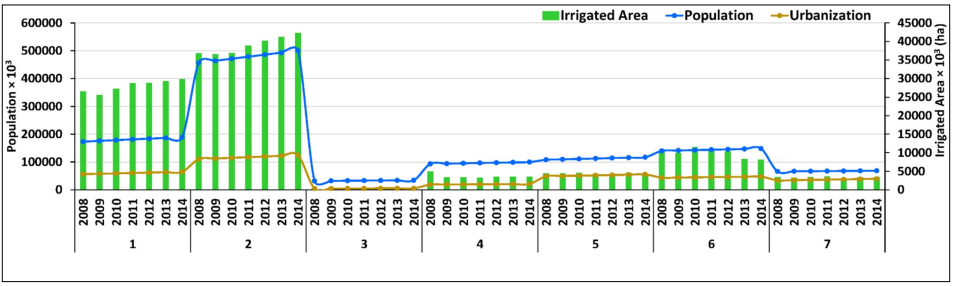

Correlation between Irrigated Area and GWS change							
Basin	1	2	3	4	5	6	7
CSR-M	0.77	0.86	0.96	0.57	0.12	0.07	0.05
JPL-M	0.71	0.86	0.99	0.54	0.21	0.07	0.02
SH	0.49	0.77	0.95	0.61	0.01	0.0002	0.09

Linear Regression (R^2) between Irrigated Area and GWS change							
Basin	1	2	3	4	5	6	7
CSR-M	0.73	0.55	0.64	-0.65	-0.34	-0.61	-0.60
JPL-M	0.75	0.78	0.66	-0.81	-0.31	-0.42	-0.59
SH	0.36	0.40	0.66	-0.54	-0.33	-0.05	-0.86

Fig. S7. Graph showing Population rise along with increase in irrigational area and Urbanization at the seven basins (Basin 1–7), having high values in Basin 1, 2. Linear Regression and Correlation is estimated between GWS an Irrigation area to validate groundwater fluctuation more thoroughly.